An improved CFD/experimental combined methodology for the calibration of empirical erosion models (Abstract Ref. number: WEAR2021_0102)

Gianandrea Vittorio Messa, Yongbo Wang, Marco Negri, Stefano Malavasi

PII: S0043-1648(21)00123-X

DOI: https://doi.org/10.1016/j.wear.2021.203734

Reference: WEA 203734

To appear in: *Wear*

Received Date: 7 September 2020

Revised Date: 8 January 2021

Accepted Date: 25 January 2021

An improved CFD/experimental combined methodology for the calibration of empirical erosion models (Abstract Ref. number: WEAR2021_0102)

Gianandrea Vittorio Messa*, Yongbo Wang, Marco Negri, Stefano Malavasi

DICA, Politecnico di Milano, Piazza Leonardo da Vinci, 32, 20133 Milano, Italy

Abstract

A significant source of uncertainty in CFD-based erosion prediction is represented by the erosion model, used to turn the particle-wall impingement characteristics into an estimate of the removal of material. In engineering computations, frequent use is made of empirical erosion models obtained by fitting the experimental results of air-solid jet impingement tests. However, since the applicability conditions of these models are often unknown or unavailable to the users of CFD codes, they are frequently misapplied, producing not only uncertain, but at times also highly inaccurate wear estimates. As part of his PhD thesis defended at the University of Tulsa in 2016, Amir Mansouri proposed a methodology to calibrate the coefficients of an empirical erosion correlation by combining experimental data and CFD results of a slurry jet impingement test. This methodology provided an effective way to overcome the criticisms of using empirical erosion models taken from the literature without facing the complexity and the high computational burden of a multiscale, physically-based approach, in which the micro-scale mechanical interactions between the particles and the target surface are resolved according to the fundamental laws of damage mechanics. The present paper presents an improved formulation of Mansouri's methodology, which not only increases the calibration accuracy of the empirical erosion equation, but also enhances the reliability of the CFD-based erosion prediction model as a whole. To this purpose, numerical simulations were supported by in-house slurry jet impingement experiments on an aluminum sample and curved Glass Reinforced Epoxy samples.

Keywords: Computational Fluid Dynamics, erosion models, direct impact test, impact erosion

1. Introduction

The numerical modelling of solid particle erosion in either dry or wet environments poses significant challenges due to the multi-scale nature of the wear process. Achieving reliable erosion estimates requires simulating the motion of the solid particles in the carrier fluid and accurately predicting the particle-wall impingement characteristics, namely, establish when and where the impacts occur, and what the velocity vector of each particle is at the stage of impingement. Achieving this task is extremely difficult for most scenarios of engineering interest, involving turbulent particle-laden flows with natural solids. The excessive computational cost of fully-resolved simulations based on the direct solution of the instantaneous flow equations, in fact, requires a number of modelling simplifications and assumptions, such as Reynolds-averaging of the governing equations, point-particle approximation, use of force models to model the interactions between the particles and the surrounding fluid (drag, pressure force, lift, etc). These modelling simplifications introduce sub-models and parameters which undermine the physical foundation of the mathematical model and, being often difficult-to-quantify, produce inherent uncertainty in the simulation results [1].

The most common approach in erosion prediction simulations based on Computational Fluid Dynamics (CFD) relies on the use of Reynolds-averaged based Eulerian-Lagrangian models, which solve for some Reynolds-averaged formulation of the fluid flow equations on an Eulerian grid of cells, and determine the

*Corresponding author. Tel. +39 02 2399 6287

Email addresses: `gianandreavittorio.messa@polimi.it` (Gianandrea Vittorio Messa), `yongbo.wang@polimi.it` (Yongbo Wang), `marco.negri@polimi.it` (Marco Negri), `stefano.malavasi@polimi.it` (Stefano Malavasi)

trajectories of a number of computational particles by integrating the Lagrangian particle equations of motion [2]. Such computational particles are often referred to as "parcels" (hereafter denoted by the letter "P"), which, in steady-state computations, are associated to a given solid mass flow rate, $\dot{m}_{\mathrm{P}}$. Eulerian-Lagrangian models make it straightforward to evaluate, for each collision between a parcel and a wall boundary, the location of the impact, the modulus of the impact velocity, $v_{\mathrm{P,imp}}$, and the angle formed by the impact velocity vector and the wall, $\theta_{\mathrm{P,imp}}$. Typically, the interactions among the particles are ignored, and often also the influence of the particles on the fluid flow. This restricts the applicability of this approach to particle-laden flows with low solid concentration, say, not higher than about one percent by volume of mixture, which are, anyway, of interest for many engineering processes in the oil and gas sector. Indeed, some investigations have been reported in which particle-particle interactions were accounted for by Lagrangian inter-particle collision models (e.g. [3, 4]): these models extend the range of applicability to higher solid content, but they still remain an exception, probably because of the increase in the computational burden of the simulations and, not secondarily, also in the number of difficult-to-estimate parameters coming into play.

At the same time, predicting solid particle erosion requires being capable to model the wear phenomenon at the micro-scale level, determining the amount of material removal from a solid body subjected to subsequent collisions from the travelling particles. This relates with the concepts of damage and fracture mechanics of solids, but a physically-based approach is rarely adopted in CFD-based erosion prediction studies. Indeed, a number of papers have been published in which Finite Element Method (FEM) or alternative methods have been employed to simulate the particle-wall impingement processes at the micro-scale and accurately predict the removal of material for specific combinations of abrasive particles and target body, but they typically ignored the influence of the fluid on the particle transport at the macro-scale level [5–7]. Such an assumption might be reasonable for high-speed, gas-particle flows, but this is not likely to be the case for liquid-solid flows. Additionally, the results obtained in these studies allow a deep understanding of physical mechanisms at the basis of material removal, but they appear to be case-specific and difficult to integrate in a CFD-based erosion prediction model.

[Figure 1 about here.]

Among CFD modelers, who mainly focus on the particle transport side of the erosion phenomenon, it is a common practice to employ simple equations to turn the particle-wall impingement characteristics into an estimate of the amount of material removal. Usually, these equations are empirically obtained from dry direct impact tests, in which a particle-laden air jet is directed against a target sample for a period of time, producing an erosion hole (Fig. 1a). The fitting of the experimental results allows expressing the following functional relation in a simple mathematical form:

$$\Delta M = \dot{M}_{\mathrm{s}} T \cdot f\left(V_{\mathrm{jet}}, \theta_{\mathrm{jet}}, \text{particle}, \text{target}\right) \tag{1}$$

where ΔM is the difference in the mass of the sample before and after the test, $\dot{M}_{\mathrm{s}}$ is the mass flow rate of abrasives leaving the nozzle, T is the duration of the test, V_{jet} is the jet bulk-mean velocity, θ_{jet} is the nozzle-to-specimen angle, and the terms "particle" and "target" are used to denote the geometrical and physical properties of the abrasives (e.g. size, shape, density, hardness etc.) and of the physical properties of target material (es. density, hardness etc.), respectively. Since the motion of the particles in a dry direct impact test is likely to be inertia-dominated, there is no dependence upon the nozzle-to-specimen distance H in Eq. 1. The same hypothesis on the fluid dynamic behavior of the particles provides a rationale for the coupling between Eq. 1 and an Eulerian-Lagrangian simulation. Since all particles are assumed to hit the target with an impact velocity approximately equal to the V_{jet} and with an impact angle approximately equal to θ_{jet}, it is argued that the same functional relationship derived at the macro-scale of the jet applies also at the micro-scale of each parcel-wall impingement, that is

$$\dot{E}_{\mathrm{P,imp}} = \dot{m}_{\mathrm{P}} \cdot f\left(v_{\mathrm{P,imp}}, \theta_{\mathrm{P,imp}}, \text{particle}, \text{target}\right) \tag{2}$$

where $\dot{E}_{\mathrm{P,imp}}$ is the mass flow rate of removed material produced by the current parcel-wall impingement.

Undoubtedly, Eq. 2 is easy to incorporate in a CFD-based erosion prediction model based on Eulerian-Lagrangian simulations, and therefore, it provides a simple way to obtain erosion estimates even for arbitrarily complex particle-laden flows in dry and wet conditions. At the same time, the validity of such approach has serious limitations because of the following reasons. Firstly, it assumes that all particles used in the experiments are equal to each other, but this is not likely to be the case for natural materials like sand. Secondly, it ignores that, from a mechanical point of view, erosive wear is a highly nonlinear process and, therefore, the mass removal from the sample is not a simple superimposition of the effects of the single impingements. Thirdly, it ignores the nonlinear time effects caused by the change in particle-laden flow field occurring as the erosion hole becomes deeper during the expriments. Fourthly, the jet velocity in dry direct impact tests is usually higher compared with the impact velocities commonly found in slurry flows; therefore, erosion models derived from dry direct impact tests are outside their calibration range when they are applied to wet particle-laden flows. Finally, and partially related with the point above, the calibration database and the applicability conditions of empirical erosion models are often unknown to CFD users and, therefore, these models are frequently misapplied, yielding results of doubtful validity. The widely used erosion model by Oka et al. [8, 9] lies in the category of empirical erosion models obtained from fitting experimental results of dry abrasive jet impingement tests. Its form is as reported in Eq. 1, where the independent variables related with "particle" and "target" are the particle diameter, the Vickers hardness of the target, and the density of the target. A set of fitting constants is provided by the experimenters for different abrasive materials (quartz, silicon carbide, glass beads). Two other parameters must be determined from load relaxation tests on the target material.

Actually, valuable attemps have been made to conjugate accurate modelling of the particle-laden flow at the macroscale with a physically based modelling of the erosive wear at the microscale. The multi-scale approach of Leguizamon et al. [10] fits precisely into this framework. The approach relies on the decoupling between the micro-scale and macro-scale processes underlying solid particle erosion. Firstly, micro-scale simulations are performed to estimate the amount of material removal caused by a train of sediments impinging against the target surface for different combinations of velocity and inclination angle. Afterwards, a macro-scale model is employed to simulate the transport of the solid particles. Each time a particle collides against a solid wall, the impact velocity and the impact angle are stored, and the eroded mass is extracted from the database of the micro-scale results previously obtained. Compared to the empirical erosion models derived from dry impingment tests, the main strength of the multi-scale approach resides in the fact that the values of mass removal are not obtained from some interpolatory formula, but from a database of physically-based simulation results. At the same time, a relevant drawback resides in the high computational cost. In order to generate a comprehensive and reliable database of micro-scale results, even limited to a specific target material, many combinations of particle impact velocities, particle impact angles, and properties of abrasive particles (density, hardness, size, shape etc.) must be simulated. In summary, the multi-scale approach of Leguizamon et al. [10] pushed the frontiers of the state-of-the-art in CFD-based erosion prediction simulations, opening the way to the possibility of predicting erosion in complex geometries, such as hydro-turbines, with a high degree of fidelity [11, 12]. At the same time, there are still some concerns on the practical usability of this approach in a typical engineering context.

For the sake of completeness, it is worth mentioning that also phoenomenological erosion models have been proposed, which lie inbetween physically-based simulations of the erosive wear at the micro-scale and fully empirical correlations derived from dry direct impact tests. Phenomenological erosion models date back to the pioneering studies of Finnie [13] and Bitter [14, 15], in which the removal of material is interpreted as a consequence of two erosion processes, namely, cutting wear and deformation wear. Cutting wear is associated with a shearing action and it mainly occurs at low impact angles. Deformation wear, instead, is typical of high impact angles, and it is associated with repeated particle impacts causing plastic deformation, hardening, and sub-surface cracking. Several phenomenological erosion models have been proposed across the last decades, but even the most recent ones (e.g. [16, 17]) deviated only slightly from the original idea and formulation of Bitter. Phenomenological erosion models allow a certain insight into the main mechanisms at the basis of the wear process, but the critical drawback resides in the high number of parameters involved. Some of these parameters are not given a precise physical meaning, whereas others are difficult-to-quantify. In the end, phenomenological erosion models have a lot of empirical content, and they are formally more complicated than fully-empirical correlations. Given the current state of the art, the authors of this paper are convinced that alternative strategies should be explored to obtain an effective erosion prediction tool for engineers.

The considerations drawn before suggest that a critical issue in CFD-based erosion prediction modelling is how to convert the particle-wall impingement characteristics into estimates of material removal. Few years ago, as part of his doctoral work at the University of Tulsa, Amir Mansouri proposed a methodology to develop an erosion model of the form of Eq. 2 starting from a combination of experimental and simulation results of a wet direct impact test. As sketched in Fig. 1b, the motion of the particles in a wet direct impact test is strongly influenced by the carrier liquid and, as a result, there is a wide range of impact velocities and impact angles. By combining the distributions of the parcel impact velocities, parcel impact angles, and parcel impact number density (that is, the number of impingements per unit wall area), as predicted by an Eulerian-Lagrangian model, and the local erosion depth, as measured by a profilometer, it is possibile to calibrate an algebraic equation representing the functional relation of Eq. 2. Mansouri described his procedure in a co-authored research article published in the Wear journal in 2015 [18], and also in a chapter of his PhD thesis, defended one year later [19]. Details of the operative procedure will be provided later in Section 4.1 of this paper. At this stage, it is simply noted that the methodology of Mansouri et al. [18] represents a practical compromise to overcome the drawbacks of empirical erosion models derived from dry direct impact tests. This methodology produces a fully empirical erosion model, which can be reasonably employed for erosion prediction in flows involving the same materials, impact velocities, and impact angles, of the wet direct impact test considered for the calibration.

In this paper, an upgraded version of the methodology of Mansouri [19] is proposed, with a twofold objective. On the one hand, the new methodology improves the accuracy of calibration of the erosion equation. On the other hand, it gives the methodology a wider scope, as the new procedure allows not only finding a case-specific erosion correlation, but also properly characterizing the effect of particle shape in the CFD-based erosion prediction model, which is one of the most significant and critical sources of uncertainty. The computational work was developed around two test cases, which were subject of an experimental campaign conducted in the Hydraulic Laboratory of Politecnico di Milano. These are the normal impingements of a slurry jet on a flat aluminium sample and on curved samples made of Glass Reinforced Epoxy (GRE). The remainder of the paper is organized in four sections, followed by the conclusions. Section 2 is dedicated to the experimental setup and methodology. Section 3 illustrates the CFD model for predicting the particle-laden flow. Section 4 starts with an overview of the original methodology of Mansouri [19], and then focuses on its upgraded formulation. Finally, in Section 5, the results for the two test cases are presented and discussed.

2. Experimental campaign

2.1. Experimental setup

The experiments were performed using the wet direct impact test facility located in the Hydraulic Laboratory of Politecnico di Milano. The setup consists of three main components, namely, a mixing tank, a centrifugal pump, and the test cabin, connected by a stainless steel piping with internal diameter of 21 mm (Fig. 2). The mixing tank has a capacity of about 270 liters, and it is equipped with a variable-speed impeller to keep the slurry in suspension. A first pipe segment connects the tank to the centrifugal pump, which is capable in reaching pressures up to 9 bar and flow rates up to about 24 m^3/h. Downstream of it, a second pipe segment is interrupted by a valve, which is used to control the flow rate. Finally, the main piping line ends inside the test cabin with a nozzle. Two nozzles have been used in the experiments, namely, a stainless steel nozzle with inner diameter of 10.4 mm for the test on the flat aluminum specimen, and a tungsten carbide nozzle with inner diameter of 8.0 mm for the tests on the curved GRE samples. The test cabin encloses also the support of the eroding samples and a screw driven system to adjust the nozzle-to-specimen distance, H, and the nozzle-to-specimen angle, θ_{jet}. In all experiments, θ_{jet} was set of 90°, the nozzle was completely submerged by water, and maintaining a constant height of water in the upper tank was possible by means of a second regulation valve placed in the flexible hose connecting the test cabin back to the mixing tank.

[Figure 2 about here.]

2.2. Measured variables and instrumentation

Controlled variables were the jet bulk-mean velocity, V_{jet}, the nozzle-to-specimen distance, H, the nozzle-to-specimen inclination angle, θ_{jet}, and the testing time, T. The jet bulk-mean velocity was inferred from the volumetric flow rate, measured using a Prosonic Flow 91WA1 ultrasonic flow metering system installed in the pipe connecting the mixing tank to the pump. The measured values of V_{jet} were combined with pressure measurements made by an absolute pressure transducer located upstream the nozzle, so that, by comparison with an experimentally-determined characteristic curve of the brand new nozzle, it was possible to monitor the degradation of the nozzle due to erosion. The nozzle-to-specimen distance and inclination angle were set manually using the screw driven system inside the test cabin; H was 12.7 mm in the test on the aluminum sample, and 20.0 mm in the tests on the GRE samples; as already mentioned, θ_{jet} was kept fixed at 90°. The testing time was measured by a standard digital clock.

The solid concentration was monitored during the tests by sampling the slurry exiting the hose connecting the test cabin to the stirred tank (point S in Fig. 2). This required a graduate flask, a balance, and a thermometer. The flask, which was used to estimate the sampling volume, had a capacity of 1.0 liter and notches every 1 ml from 990 ml to 1010 ml, with an accuracy of 0.4 ml. The weight of the sampling volume was calculated as the difference between the weight of the flask with the sampling volume and that of the empty and dry flask. The flask with the sampling volume was weighted using a laboratory balance (PCE-BS 3000) with accuracy of 0.3 g. The empty and dry flask was previously weighted with a balance with a much higher accuracy and periodically checked through the test sessions. Finally, the thermometer, having accuracy of 0.5° C, was used to measure the temperature of the sample. By assuming the absence of slip between the solid particles and the carrier fluid and the representativeness of the sampling point, the solid concentration at the nozzle exit, C, could be obtained from the density of the slurry, as follows:

$$\frac{M_{\mathrm{sample}}}{W_{\mathrm{sample}}} = \rho_{\mathrm{l}}(1 - C) + \rho_{\mathrm{p}} C \tag{3}$$

where M_{sample} is the mass of the sample, calculated as a difference between the mass of the filled flask and that of the empty flask, W_{sample} is the volume of the sample, obtained from the notches of the flask, ρ_{l} is the density of the carrier liquid, inferred from temperature using a standard correlation for water [20], and ρ_{p} is the density of the solid particles, provided by the retailer. The mass loss of the sample caused by erosion, ΔM, was obtained by weighting the sample before and after the test using a Mettler Toledo AE200 balance, with accuracy of 0.3 mg and full-scale value of 200 g. In order to determine the shape of the erosion crater, the surface of the samples at the end of the tests was scanned with a resolution grid of 0.5 mm in both directions. To this aim, use was made of a laser-triangulation CMOS CCD profilometer, in which the laser was secured to two axes controlled by servomotors, and an optoelectronic system integrated with a digital signal processor measured the displacements with respect to a target without contact with the object, by means of a triangulation method (measuring range of 50 mm; linearity of ±0.2%; static resolution of 5 μm, 25 μm dynamic resolution, 1 kHz measurement rate). For all tests, the values of ΔM obtained from weight measurements were about 20-30% larger than the corresponding estimates calculated by multiplying the density of the target material by the volume of the erosion hole, which, in turn, was obtained by numerically integrating the data acquired with the profilometer. Such deviation was judged satisfactory by the authors, considering that errors might have occurred in estimating the surface of the undamaged specimens from the profilometer data.

2.3. *Sources of uncertainty in the experimental results*

Uncertainty was evaluated for all experimental parameters coming into play in the comparison with the numerical simulations. Starting from to the indications provided in the datasheet of the flowmeter, the uncertainty of the jet bulk-mean velocity, V_{jet}, was estimated as ±2.4% of the measued value. The nozzle-to-specimen distance, H, was set by turning a longitudinal screw manually, and verified using a caliber with a tolerance of 0.05 mm. The nozzle-to-specimen angle, θ_{jet}, was set by turning another screw and verified with a goniometer, and it reasonable to assume an uncertainty of about ±1°.

The uncertainty in the solid volume fraction at the nozzle outlet was a combination of three factors. Firstly, the propagation of the uncertainties of the other terms in Eq. 3, which yielded $\pm 3 \cdot 10^{-4}$. Such estimate was obtained by applying the error propagation law to Eq. 3, considering that uncertainty in the particle density could not be quantified based on the only information available, that of the water density was found negligible given the slight influence on temperature, and, finally, uncertainties in M_{sample} and W_{sample} were of the order of ±0.03% and ±0.1%, respectively. A second source of uncertainty in C was due to the fact that the amount of solids carried along with the flow varied with time because particle accumulation and resuspension could not be completely avoided. Following the sampling procedure illustrated in Section 2.2, the concentration was determined approximately every two-to-three minutes during each test, showing a variability with respect to the time-averaged values lower than $\pm 7 \cdot 10^{-4}$. Finally, the representativeness of the sampling point should be taken into account. This aspect is not simple to investigate from a quantitative point of view, but, since the solids are unlikely to deposit in the test cabin due to the high slope of its bottom wall, the solid concentration at the sampling point S in Fig. 2 should not be too different from the value at the nozzle outlet. Based on the above considerations, it seems reasonable to expect, for each experimental test, an uncertainty of $\pm 1 \cdot 10^{-3}$ on the solid volume fraction. This value is in agreement with the estimate of Mansouri et al. [21] in previous wet direct impact tests. Note that, as the testing time increases, the calculated average concentration value appears more and more reliable, as the higher number of samples reduces the fluctuations in the solid volume fraction.

The overall measurement accuracy of the specimen mass was calculated considering the repeatability (three times the standard deviation), which was 3.5 mg. Before each measurement, the specimen was cleaned with an alcohol wet cloth. The much larger value of repeatablity (3.5 mg) compared to the accuracy of the balance (0.3 mg) was probably due to powder or micro-exfoliation when handling the specimens. The accuracy of the erosion depth measurements was estimated as the product between the linearity and the measuring range of the profilometer, that is, ±0.2% · 50 mm=0.1 mm.

Finally, other sources of uncertainty are related with the properties of the solid particles. As already mentioned, the particle density was not measured but reference was made to the value indicated by the retailer. Nonetheless, application of the error propagation law showed that an error even up to 100 kg/m^3

does not significantly affect the error on solid volume fraction, which is mostly influenced by the error on the measurement of the sampling volume. Before running the tests, a rough sieve analysis was performed to determine the particle size distribution of the coarsest sand used in the experiments, which was found in reasonable agreement with the data provided by the retailer. Since it is well known that, in closed setups involving a recycled use of the solids, the size and shape of the particles may vary with time due to particle breaking and rounding [22], the sieve analysis was repeated after about 3 and 6 hours of operation of the loop, suggesting a decrease in the mean value, $d_{p,50}$, as follows: $d_{p,50}$=0.371 mm (new sand), $d_{p,50}$=0.348 mm (after 3 hours and 25 minutes of operation), $d_{p,50}$=0.324 mm (after 6 hours and 30 minutes of operation). Qualitative comparison of microscope images of the new and the used sand grains indicated no significant variation in grain shape. As it will be discussed later, the progressive reduction of particle size was subject of concern when numerically simulating the experiments. The key elements of the uncertainty analysis described in this section are summarized in Table 1.

[Table 1 about here.]

2.4. *Materials and testing conditions*

Two different combinations of target specimen and abrasive particles were investigated. Firstly, preliminary tests were run on samples made of aluminum alloy EN AW-6082, whose density was assumed as 2700 kg/m^3 based on indications received from the retailer. The specimens were prisms with rectangular cross-section and side lengths of 80 mm x 60 mm x 5 mm. In these tests, the abradant was a coarse silica sand with the following properties, as obtained from the data provided by the retailer: particle density 2500 kg/m^3, $d_{p,10}$=0.25 mm, $d_{p,50}$=0.35 mm, and $d_{p,90}$=0.46 mm.

Other experiments were conducted on samples made of a Glass Reinforced Epoxy (GRE) composite. The specimens were obtained by cutting a circular pipe and, therefore, they have a surface curvature, which is likely to affect the fluid dynamic behavior of the particle-laden flow. Their dimensions are indicated in Fig. 3a. In order to be able to install the curved samples into the test cabin, a special holder was designed and manufactured, as shown in Fig. 3b. The density of the GRE was 2050±50 kg/m^3, as estimated from measuring the weight and the volume of the samples. In the GRE tests, use was made of fine silica sand with density 2500 kg/m^3, and size distribution defined by $d_{p,10}$=0.075 mm, $d_{p,50}$=0.125 mm, and $d_{p,90}$=0.2 mm. As for the coarse sand, also the particle properties of the fine sand reported above were obtained from the datasheets provided by the retailer.

[Figure 3 about here.]

The experiments conducted on the EN AW-6082 specimens referred to a single testing condition, namely, V_{jet}=35.53±0.71 m/s, θ_{jet} = 90±1°, C = 0.0085±0.001, and T = 5 min. In this experiment, the abradant was the coarse silica sand described above. Conversely, the GRE experiments was carried out using the fine sand. The jet velocity was around 35 m/s, the nozzle-to-specimen angle was 90 ± 1°, the solid volume fraction was in the range 0.0076 ÷ 0.0085, and the duration of the tests varied from 5 to 30 minutes. Repeatability tests were conducted for some of the tested conditions, yielding, in all cases, successful results. Relevant details concerning the testing conditions are summarized in Table 2.

[Table 2 about here.]

3. CFD modelling of the particle-laden flow

3.1. *Eulerian-Lagrangian equations*

Owing to the relatively low solid volume fraction, and on the grounds of the findings obtained in a previous study [1], one-way coupling was assumed between the phases, thereby neglecting the influence of the particles on the carrier fluid and any type of particle-particle interactions. As a result, it was possible to decouple the solution of the carrier fluid flow and the calculation of the parcels' trajectories, with considerable reduction of the simulation time. Firstly, the single-phase formulation of the Reynolds Averaged Navier-Stokes equations was solved to determine the time-averaged pressure, P, and the velocity vector, $\boldsymbol{U}$, of the carrier liquid [23]. These equations were coupled with the built-in Reynolds Stress Model (RSM) in Ansys Fluent with default settings [24], which is expected to be more accurate than eddy viscosity based turbulence models in reproducing the anisotropic turbulent flow occurring when a jet impinges a surface.

The scalable wall function option available in Ansys Fluent was employed to model the turbulence characteristics in the near-wall cells. Secondly, the trajectories of the parcels were determined one after the other by solving the following Lagragian equation of motion for each parcel

$$m_\mathrm{p}\frac{\mathrm{d}\boldsymbol{v}_\mathrm{P}}{\mathrm{d}t} = \boldsymbol{F}_\mathrm{d} + \boldsymbol{F}_\mathrm{l} + \boldsymbol{F}_\mathrm{p} + \boldsymbol{F}_\mathrm{vm} \tag{4}$$

where m_p is the mass of a particle, and the four terms on the right hand side indicate the forces acting on a parcel, which are drag force, lift force, pressure gradient force, and virtual mass force, respectively. Other forces, such as gravity, buoyancy, and history force, were ignored because they are expected to play a minor role in the case studies considered. The four forces in Eq. 4 were calculated as

$$\boldsymbol{F}_\mathrm{d} = \frac{1}{2}\rho_\mathrm{l}C_\mathrm{d}\left(\pi\frac{d_\mathrm{p}^2}{4}\right)|\boldsymbol{u}_\mathrm{@P} - \boldsymbol{v}_\mathrm{P}|\,(\boldsymbol{u}_\mathrm{@P} - \boldsymbol{v}_\mathrm{P}) \tag{5}$$

$$\boldsymbol{F}_\mathrm{l} = 3.0844J^*\frac{m_\mathrm{p}}{\rho_\mathrm{p}d_\mathrm{p}}\sqrt{\frac{\nu_\mathrm{l}}{|\Omega_\mathrm{l,@P}|}}\cdot[\Omega_\mathrm{l,@P}\times(\boldsymbol{U}_\mathrm{@P} - \boldsymbol{v}_\mathrm{P})] \tag{6}$$

$$\boldsymbol{F}_\mathrm{p} = -\frac{m_\mathrm{p}}{\rho_\mathrm{p}}\nabla P_\mathrm{@P} \tag{7}$$

$$\boldsymbol{F}_\mathrm{vm} = C_\mathrm{vm}\rho_\mathrm{l}\frac{m_\mathrm{p}}{\rho_\mathrm{p}}\left(\frac{\mathrm{d}\boldsymbol{v}_\mathrm{P}}{\mathrm{d}t} - \frac{\mathrm{d}\boldsymbol{U}_\mathrm{@P}}{\mathrm{d}t}\right) \tag{8}$$

where t is the Lagrangian integration time, $\boldsymbol{v}_\mathrm{P}$ is the instantaneous parcel velocity, d_p is the volume-equivalent particle diameter, that is, the diameter of a sphere having the same volume of the actual particle, $\boldsymbol{u}$ is the instantaneous velocity vector of the liquid, ν_l is the kinematic viscosity of the liquid, $\Omega_\mathrm{l} = \nabla\times\boldsymbol{U}$ is the mean vorticity of the liquid, C_d, J^*, and C_vm are dimensionless coefficients, and the subscript @P means that $\boldsymbol{u}$, $\boldsymbol{U}$, Ω_l, and ∇P are interpolated at the current parcel position. The drag coefficient, C_d, is obtained from the empirical correlation of Haider and Levenspiel [25], which expresses C_d as function of the local mean parcel Reynolds number, $Re_\mathrm{P} = |\boldsymbol{U}_\mathrm{@P} - \boldsymbol{v}|d_\mathrm{p}/\nu_\mathrm{l}$, and the particle spherical coefficient, φ, which accounts for the effect of particle shape and it is defined as the ratio between the surface area of the volume-equivalent sphere and the actual surface area of the particle. Recommended values for φ are 0.66, 0.76, and 0.86 for highly sharp, nearly rounded, and fully rounded grains [1], whereas a unit value applies to the ideal case of perfectly spherical particles. The coefficient J^* in Eq. 6 was quantified through an empirical correlation provided by Mei [26], which arises as an extension of the well known Saffman's formula to finite particle Reynolds number and was implemented in the Ansys Fluent code through a User Defined Function. Finally, the virtual mass coefficient, C_vm, was set to 0.5, as commonly assumed in the literature.

Eq. 4 was solved in conjunction with another ordinary differential equation for the parcel position vector, $\boldsymbol{r}_\mathrm{P}$, as follows:

$$\frac{\mathrm{d}\boldsymbol{r}_\mathrm{P}}{\mathrm{d}t} = \boldsymbol{v}_\mathrm{P} \tag{9}$$

and the numerical integration of the two equations yielded, for a discrete set of Lagrangian time instants, the parcel position vector and the instantaneous parcel velocity vector. The instantaneous fluid velocity vector, $\boldsymbol{u}$, which appears in Eq. 5, was evaluated from the RANS solution using a discrete random walk stochastic model embedded in the Ansys Fluent code [24], leaving all default settings. Relevant details on the settings of the Eulerian-Lagrangian model are summarized in Table 3.

[Table 3 about here.]

3.2. Computational domain and boundary conditions

A sketch of the computational domain, including the boundary conditions, is shown in Fig. 4 for the curved GRE specimen case. The domain includes the nozzle with its actual thickness, modeled as a straight pipe with length equal to 10 nozzle inner diameters, the specimen with its clamps, and the surrounding environment (Fig. 4a). A similar setup was defined for the flat aluminium case, where the target wall was a plane circle surronding the rectangular specimen (as in Fig. 4a of the earlier paper [1]).

[Figure 4 about here.]

Boundary conditions were inlet, outlet, and solid walls. At the inlet, a fully-developed mean axial velocity profile was specified [27], its mean value being V_{jet}, whereas the two other mean velocity components and all turbulence parameters were set as zero. In order to define the parcels' initial conditions, the mass flow rate associated to each parcel was calculated first. Particularly, all parcels were attributed the same mass flow rate, $\dot{m}_{\mathrm{P}}$, determined in such a way to produce the desired solid volume fraction at the nozzle exit, that is,

$$\dot{m}_{\mathrm{P}} = \frac{\rho_{\mathrm{p}} C V_{\mathrm{jet}} \pi \frac{d^2}{4}}{N_{\mathrm{P}}} \tag{10}$$

where d is the inner diameter of the nozzle, and N_{P} is the total number of tracked parcels. The inlet boundary was triangulated, and the averaged fluid velocity and liquid mass flow rate were calculated for each triangle. The number of injected parcels from each triangle was proportional to the local liquid mass flow rate, their initial positions were extracted randomly from a uniform probability distribution over the triangle, and their initial velocities were equal to the local averaged fluid velocity. In Ansys Fluent, the particle size associated to each parcel must also be specified at the inlet section. As it will be discussed later, this was achieved by sampling the values from a log normal probability distribution. At the outlet, the mean gauge pressure of the fluid and the normal gradient of all other fluid-related variables were specified as zero, whereas the parcels simply leave the domain. At the walls, the fluid velocity is zero and, as already mentioned, the scalable wall function option is employed to model the turbulence characteristics in the near-wall cells. The parcels rebound when they hit a solid wall. The normal and tangential parcel velocity components after impingement are related with the corresponding incident values through two restituion coefficients, which are expressed as polynomial functions of the parcel impact angle through the empirical correlations of Forder et al. [28]. As it will be detailed later in Section 4.2, following an earlier study of two of the authors of this paper [29], the parcel-wall impingement characteristics (velocity, angle, and position) were not evaluated at a distance from the wall equal to half particle size, as an approximate way to take the finite particle size into account in the point-particle framework. This was achieved through a User Defined Function.

3.3. CFD solution strategy

The numerical simulations were performed using the commercial code Ansys Fluent version 19.2, complemented with User Defined Functions. As already mentioned, owing to the one-way coupling regime assumption, the single-phase flow of the carrier liquid was calculated first by solving the RANS equations in the Eulerian, cell-based formulation. Unstructured tetrahedral meshes was initially created, and then converted into polyhedral meshes in Ansys Fluent for speeding up the simulation time: as a rule of thumb, in fact, the number of cells in a polyhedral mesh can be close to one fifth of that of the original tetrahedral mesh. Fig. 5 shows the spatial discretization on a restricted view of the mid plane in the case of the curved GRE specimen. The sketch clearly reveals that the cells are densified in the core region of the domain, which is more prone to particle-wall impingements. Additionally, an inflation layer is added adjacent to the surface of the specimen and the inner surface of the nozzle, based on a first layer thickness of 0.05 mm. An extensive mesh sensitivity study was performed for the calibration case presented in Section 5.2, referring to the normal jet impingement on a GRE specimen with $V_{\mathrm{jet}} = 35.53$ m/s, $C = 0.0085$, and $T = 5$ min, the target parameter being the local mean fluid velocity profile along a line near the sample surface. The solutions calculated on meshes with 0.18, 0.41, 0.72, 1.45, and 2.11 million elements were compared, and substantially grid-independent results were obtained with the 1.45 million cells. Starting from the results of this test case, the mesh sensistivity analysis was repeated for all other computation domains, finding that, in the flat aluminum specimen case, about 1.26 million cells were enough to attain mesh independence. Note that, since the parcel-wall impingement characteristics were not evaluated at the wall but at a distance upstream of it equal to half particle size (Section 4.2), they were only minorly affected by the near-wall mesh resolution and inflation layer properties. For the numerical solution of the RANS equations, a coupled pressure-velocity scheme was used, with Green-Gauss Node-Based gradient discretization, PRESTO! pressure discretization, and Second Order Upwind schemes applied to all other solved variables. The convergence criterion was that the normalized unscaled residuals must drop to below 10^{-4} and, additionally, the area-averaged wall skin friction factor of the specimen was verified to become constant. The under-relaxation factors were left to their default values.

[Figure 5 about here.]

Once the carrier fluid flow field was calculated, the parcel trajectories were determined sequentially through the integration of the Lagrangian equations of motion. This was achieved through the DPM model available in Ansys Fluent in the steady-state particle tracking mode, without accounting for the effect of the parcels on the continuous phase. The default numerical settings of the DPM were used. The number of tracked parcels was 50000, high enough to attain significant parcel-wall impingement statistics. A brief sensitivity analysis was made for the flat specimen case discussed in Section 5.1, which indicated that even doubling the number of trajectories did not produce any significant change to the curve fitting coefficients. Table 4 provides the key details on the numerical settings of the CFD model.

[Table 4 about here.]

4. Methodology for erosion model calibration

4.1. The original methodology of Mansouri [19]

The methodology proposed by Mansouri allows calibrating an empirical erosion model having the following form

$$\dot{E}_{\mathrm{P,imp}} = \dot{m}_{\mathrm{P}} F_{\mathrm{s}} K \cdot v_{\mathrm{P,imp}}^{n} f\left(\theta_{\mathrm{P,imp}}\right) \tag{11}$$

by combining the experimental measurements and the simulation results of a wet direct impact test (Fig. 1b). In Eq. 11, F_{s} is a dimensionless coefficient related with particle shape, equal to 0.2, 0.53, and 1.0 for fully rounded, nearly rounded, and fully sharp grains, respectively, K is a material-related constants, which includes also the influence of particle size, n is a velocity exponent, and $f\left(\theta_{\mathrm{P,imp}}\right)$ is a two-parameters impact angle function, as follows,

$$f\left(\theta_{\mathrm{P,imp}}\right) = \left(\sin\theta_{\mathrm{P,imp}}\right)^{b1} \cdot \left(1.5 - \sin\theta_{\mathrm{P,imp}}\right)^{b2} \tag{12}$$

The idea of Mansouri, as presented in his PhD thesis [19], is to divide the target wall into N_{cells} surface cells and apply Eq. 11 is applied at the scale of each cell. This yields

$$\dot{E}_i = \dot{M}_i F_{\mathrm{s}} K \cdot \langle v_{\mathrm{P,imp}} \rangle_i^n f\left(\langle \theta_{\mathrm{P,imp}} \rangle_i\right) \tag{13}$$

where the subscript i means that the following quantities refer to the generic cell: $\dot{E}_i$ is the total mass flow rate of removed material, $\dot{M}_{\mathrm{i}}$ is the impinging mass flow rate, equal to the product of the number of impingements and the mass flow rate associated to each parcel, $\langle v_{\mathrm{P,imp}} \rangle_i$ is the average of the parcel impact velocities, and $\langle \theta_{\mathrm{P,imp}} \rangle_i$ is the average of the parcel impact angles. After dividing by the product of the target material density, ρ_{t}, and the area of the cell, ΔA_i, and multiplying by the testing time, T, the area-averaged erosion depth of each cell, $\langle h \rangle_i$, can be obtained as

$$\langle h \rangle_i = \frac{\dot{E}_i T}{\rho_{\mathrm{t}} \Delta A_i} = \frac{\dot{M}_i F_{\mathrm{s}} K \cdot \langle v_{\mathrm{P,imp}} \rangle_i^n f\left(\langle \theta_{\mathrm{P,imp}} \rangle_i\right)}{\rho_{\mathrm{t}} \Delta A_i} \cdot T \tag{14}$$

and, finally, Eq. 14 can be rearranged as

$$K \cdot f\left(\langle \theta_{\mathrm{P,imp}} \rangle_i\right) = \frac{\langle h \rangle_i}{T \cdot F_{\mathrm{s}} \cdot \langle v_{\mathrm{P,imp}} \rangle_i^n} \cdot \frac{\rho_{\mathrm{t}} \Delta A_i}{\dot{M}_i} \tag{15}$$

For each cell i, the erosion depth $\langle h \rangle_i$ can be measured using a profilometer. Conversely, $\dot{M}_i$, $\langle v_{\mathrm{P,imp}} \rangle_i$, and $\langle \theta_{\mathrm{P,imp}} \rangle_i$ are difficult to evaluate experimentally, but they can be easily estimated from an Eulerian-Lagrangian CFD simulation. By combining the numerical and experimental results, a list of N_{cells} pairs of coordinates $[\langle \theta_{\mathrm{P,imp}} \rangle_i, K \cdot f(\langle \theta_{\mathrm{P,imp}} \rangle_i)]$ can be determined, and the coefficients K, $b1$, and $b2$ can be obtained by applying some regression procedure. This requires the velocity exponent n to be known, but this aspect has not completely clarified by Mansouri et al. [18], who simply assumed $n = 2.4$ based on previous experimental findings and did not provide any criteria for deciding the value of this parameter. According to the authors, this aspect deserves more attention but, unfortunately, the experimental data currently available did not allow gaining more insight. Therefore, this task was shelved for future research, and, in this study, the value of n was left to 2.4. A flowchart of the original methodology of Mansouri [19] is shown in Fig. 6.

[Figure 6 about here.]

4.2. *An improved methodology*

Three main modifications were made to the methodology of Mansouri [19] in order to improve the accuracy of erosion model calibration and widening its scope.

Firstly, the particle shape coefficient F_s is included in the calibration constant K, and, therefore, the formulations of the erosion model applied at the single impact scale and at the cell scale are, respectively,

$$\dot{E}_{\mathrm{P,imp}} = \dot{m}_{\mathrm{P}} K \cdot v^{n}_{\mathrm{P,imp}} f\left(\theta_{\mathrm{P,imp}}\right) \tag{16}$$

and

$$\dot{E}_i = \dot{M}_i K \cdot \langle v_{\mathrm{P,imp}} \rangle^{n}_{i} f\left(\langle \theta_{\mathrm{P,imp}} \rangle_i\right) \tag{17}$$

Although this change might appear purely formal, it is indeed important for several inter-related reasons, as follows. When combining the current Eulerian-Lagrangian model with the original erosion model formulation of Mansouri, particle shape is accounted for via two parameters. The former is the particle spherical coefficient, φ. This parameter appears in the drag coefficient correlation of Haider and Levenspiel [25] to quantify the influence of particle shape on the resistence encountered by the particles travelling in the carrier fluid, and, therefore, it affects the parcel trajectories and the parcel-wall impingement characteristics. The latter parameter is the coefficient F_s in the erosion model (Eq. 11), which quantifies the effect of particle shape on the mass removal produced by a single impinging particle, for the same impact velocity and angle. As already said, recommended values of φ and F_s for fully sharp, nearly rounded, and fully rounded grains are (0.66, 0.76, 0.86) and (1.0, 0.53, 0.2), respectively. However, these parameters should not be treated as independent with each other, as they are associated with the same geometrical property of the grains. Avoiding the explicit appearence of F_s stresses this aspect.

In addition, particle shape is difficult to quantify for natural sands, and, therefore, φ (and F_s) are critical features of a CFD-based erosion prediction model. An earlier study by Messa and Malavasi [1] showed that, when simulating a wet direct impingement test, the value of φ has a significant influence on the particle-wall impingement characteristics. Based on the above considerations, it is here proposed to use the consistency between the map of the particle-wall collisions, obtained from the CFD simulation, and the shape of the erosion hole found in the experimental test as a criterion to decide the value of φ within the triplet (0.66, 0.76, 0.86).

The last reason why it was decided to include F_s in the calibration constant K is to make the applicability limits of the calibrated model evident. In fact, leaving F_s at the denominator of Eq. 15, as Mansouri et al. [18] did, implies that the calibration constants K, $b1$, and $b2$ would be valid for different particle shapes, since the effect of this parameter could be accounted for a posteriori by changing F_s. Instead, it is here recommended to employ the calibrated formula only for cases involving the same type of abrasive particles, also because particle shape, particle size and particle material are usually strongly interrelated, and, therefore, it seems reasonable to include all these parameters into K, $b1$, and $b2$.

The second modification made to Mansouri's strategy is to change, in the analogous of Eq. 15 for the new formulation, the term related with the impact velocity from $\langle v_{\mathrm{P,imp}} \rangle^{n}_{i}$ to $\langle v^{n}_{\mathrm{P,imp}} \rangle_i$. The rationale behind this change is to make the calibration of the model more consistent with the post-processing of the parcel-wall impingement characteristics through the E-CODE, which is the in-house MATLAB library for erosion calculation developed with the authors' research group. In the E-CODE, each impact point is associated to the centroid of the nearest surface cell, and the erosion model in the form of Eq. 11 is applied to find the mass flow rate of removed material caused by the current impingement. The sum over all impingements associated to the same cell yields the mass flow rate of removed material of that cell, $\dot{E}_i$. Note that, for the sake of clarity, the generic cell is denoted once again by the subscript i, since the surface discretization in the E-CODE is the same considered when illustrating the calibration methodology in Section 4.1; therefore, the number of impingements occurring in that cell is referred to as $N_{\mathrm{imp},i}$. Since each cell is attributed a single erosion depth, this can be interpreted as the area-averaged value over the cell. Using Eq. 16, the area-averaged erosion depth of cell i after a time T, called $\langle h \rangle_i$, can be obtained as:

$$\langle h \rangle_i = \frac{\dot{E}_i}{\rho_t \Delta A_i} T = \frac{T}{\rho_t \Delta A_i} \cdot \left[\sum_{P=1}^{N_{\mathrm{imp},i}} \dot{m}_{\mathrm{P}} K v^{n}_{\mathrm{P,imp}} f\left(\theta_{\mathrm{P,imp}}\right) \right] \tag{18}$$

and the equation above can be rearranged as:

$$\langle h \rangle_i = \frac{\dot{M}_i K \langle v^{n}_{\mathrm{P,imp}} f\left(\theta_{\mathrm{P,imp}}\right) \rangle_i}{\rho_t \Delta A_i} \cdot T \tag{19}$$

where the impinging mass flow rate over the cell is calculated as $N_{\mathrm{imp},i}\dot{m}_{\mathrm{P}}$. Clearly, it is not possible to turn Eq. 19 into an equation for the product $K \cdot f(\langle\theta_{\mathrm{P,imp}}\rangle_i)$, since the area-averaging operator is applied to the term $v^n_{\mathrm{P,imp}} f(\theta_{\mathrm{P,imp}})$. However, if the following assumption is made:

$$\langle v^n_{\mathrm{P,imp}} f\left(\theta_{\mathrm{P,imp}}\right)\rangle_i \approx \langle v^n_{\mathrm{P,imp}}\rangle \cdot f\left(\langle\theta_{\mathrm{P,imp}}\rangle_i\right) \tag{20}$$

then, an explicit expression for $K \cdot f(\langle\theta_{\mathrm{P,imp}}\rangle_i)$ can be found, as follows,

$$K \cdot f\left(\langle\theta_{\mathrm{P,imp}}\rangle_i\right) = \frac{\langle h\rangle_i}{T \cdot \langle v^n_{\mathrm{P,imp}}\rangle_i} \cdot \frac{\rho_t \Delta A_i}{\dot{M}_i} \tag{21}$$

and the formula here above is used instead of Eq. 15 to find the calibration constants K, $b1$, and $b2$. Indeed, Eq. 20 does not have a clear theoretical justification, but it represents a practical way to make the area-averaged approach of Mansouri's procedure consistent with the parcel-based approach at the basis of the E-CODE. In order to obtain the original formulation of Mansouri, a second assumption should be made alongside with Eq. 20, that is, $\langle v^n_{\mathrm{P,imp}}\rangle_i \approx \langle v_{\mathrm{P,imp}}\rangle^n_i$. However, not only this additional approximation would be further unjustified from a theoretical point of view, but it would also have an adverse effect on the calibration accuracy, as it will be shown later in Section 5.2. Finally, for the sake of completeness, it is mentioned that, in the E-CODE, the overall mass loss after a given time T is obtained as

$$\Delta M = \sum_i \dot{E}_i T \tag{22}$$

where the summation is over all surface cells.

The last difference between the current investigation and the works by Mansouri [18, 19] is not related with the calibration procedure in itself, but, rather, in the evaluation of the parcel-wall impingement characteristics from the output of the Eulerian-Lagrangian CFD simulation.

Eulerian-Lagrangian models for engineering calculations, such as the one employed in this study, rely on the already mentioned point-particle approximation, in which the parcels are treated as point sources of momentum with zero dimension. As a result, the integration of the parcel trajectories is performed up to the wall boundary and the impingement characteristics (that is, position of the impact, impact velocity, and impact angle) are evaluated at the wall. As discussed by two authors of this paper in a previous study [29], such computational procedure seriously affects the reliability of the CFD-based erosion prediction model for two reasons. On the one hand, it produces an underestimation of the impact velocity, because the high drag experienced by the parcels in the near-wall region, where the fluid velocity is very low owing to the presence of the boundary layer, is a mere consequence of ignoring the actual size of the solids. On the other hand, it makes the particle-wall impingement characteristics strongly dependent on the mesh resolution close to the wall as well as on the near-wall treatment approach used. Since a fully-resolved treatment of the solid phase would result in prohibitive computational cost, two practical strategies were proposed by reseachers.

Zhang et al. [30] recommended to use different mesh sizes and different near-wall treatment methods according to the size of the particles. Undoubtedly, this approach is very easy to implement, but it suffers from lack of applicability when considering particle-laden flows with broad grain size distributions. Conversely, Messa and Wang [29] proposed to evaluate the parcel-wall impingement characteristics at the particle centroid, that is, at a distance from the wall equal to half particle diameter (Fig. 7). Note that this alternative approach does not impose the particle rebound to occur at the particle centroid, but it extracts from a point-particle trajectory the parcel position, velocity and angle half particle diameter away from the wall, and take these values as the parcel-wall impingement characteristics to be used in the erosion calculations. The method by Messa and Wang [29], employed in this study, has a clear physical meaning, and it is applicable to either mono-dispersed or poly-dispersed particle-laden flows. Additionally, it makes the parcel-wall impingement characteristics (and, therefore, the erosion estimates) less sensitive to the near-wall mesh resolution and wall treatment method compared to the traditional point-particle method. At the same time, its implementation in the Ansys Fluent code required writing a library of UDFs.

[Figure 7 about here.]

The flowchart of the improved methodology is shown in Fig. 8. Note that the upgraded procedure allows overcoming some limitations of CFD-based erosion prediction highlighted by Parsi et al. [31], namely, the problems with commercial particle tracking subroutines which rely on the point-particle approximation, the strong influence of the mesh on the erosion predictions, and the uncertainty related with the value of the particle spherical coefficient.

[Figure 8 about here.]

4.3. A formulation for statistically axi-symmetric flows

The first case study considered in this paper is the normal impingement of a slurry jet on a flat specimen, in which the particle-laden flow is statistically axi-symmetric, and, therefore, also the erosion hole is axi-symmetric as well. When addressing this test case, use was made of a formulation of the calibration methodology which is valid only for statistically axi-symmetric flows, in which the parcel-wall impingement characteristics and the local erosion depth depend only on a radial coordinate measured from the center of the specimen. In the axi-symmetric formulation, the surface of the specimen is no longer subdivided in square cells but, rather, into N_{rings} concentric rings with radius r_i and thickness Δr_i (Fig. 9).

[Figure 9 about here.]

When the upgraded methodology, illustrated in Section 4.2, is applied at the ring scale, Eq. 21 becomes:

$$K \cdot f\left(\langle\theta_{\text{P,imp}}\rangle_{\text{ring},i}\right) = \frac{\langle h\rangle_{\text{ring},i}}{T \cdot \langle v^n_{\text{P,imp}}\rangle_{\text{ring},i}} \cdot \frac{\rho_t \Delta A_{\text{ring},i}}{\dot{M}_{\text{ring},i}} \tag{23}$$

where the new subscript “ring, i” means that all quantities refer to the generic ring with center radius r_i. Provided that Δr_i is sufficiently small, the ring area $\Delta A_{\text{ring},i}$ could be estimated as $2r_i\pi\Delta r_i$.

Applying Eq.23 requires evaluating the ring-based values of an experimentally-determined variable, that is, the ring-averaged erosion depth, as well as of three parameters obtained from the CFD simulation, namely, the ring-averaged parcel impact velocity elevated to power n, the ring-averaged parcel impact angle, and the total impinging mass flow rate in each ring. Using the E-CODE, evaluating the parcel wall impingement characteristics at the scale of the ring simply required implementing in the MATLAB subroutine a proper discretization of the specimen surface. Conversely, some interpolation of the experimentally-determined erosion depth values was necessary, since these data were acquired by the profilometer on a cartesian grid of measuring points.

Obviously, the cell-based methodology might be directly applied also to statistically axi-symmetric flows. The reason behind the authors' choice to develop a case-specific, ring-based formulation is twofold. On the one hand, expressing the statistics of the parcel-wall impingements as well as the erosion depth as a function of a single space coordinate, that is, the radial one, appears the most straightforward choice and makes the results more easily accessible and interpretable. On the other hand, it is easier to get statistically significant statistics on a large ring rather then on a small elementary square cell. That is, taking advantage of the known axi-symmetric behavior of the mean flow, it is possible to reduce the number of tracked parcels and, therefore, the computational burden of CFD simulation and data processing.

5. Results and discussion

The experimental and numerical results obtained in the present study are reported and discussed hereafter. Particularly, in Section 5.1, the calibration of the erosion correlation for a normal jet impingement against a flat aluminum specimen is described, as performed adopting the ring-based formulation presented in Section 4.3. Section 5.2 illustrates the development of an erosion correlation from the case of normal jet impingement against a curved GRE specimen. Since the phenomenon is no longer axisymmetric, use was made of the more general cell-based approach. Although this study almost entirely focused on the calibration of the erosion model, examples of application of the calibrated formula to GRE experiments with longer testing times are presented and discussed.

Before illustrating the results, it is noted that, for different reasons, both the experimentally-measured and the numerically-obtained erosion depth distributions had to be filtered a posteriori to smooth out noise. In the experimental data, such noise mainly arose from measurement errors and/or lack of complete control of the experimental conditions, whereas, in the numerical solution, it was a consequence of the discrete nature of particle tracking in Eulerian-Lagrangian models, in addition to the fact that, as already explained in Section 4.2, the E-CODE calculates the erosion of each surface cells considering only the impacts occurring in that cell, and it does not perform weight-averaging of the impacts in neighboring cells as well. After testing different types of smoothing filters implemented in MATLAB, it was decided to employ a nine-point moving average filter. Another aspect to consider when processing the experimental data was that the point of intersection between the nozzle axis and the surface of the specimen, virtually corresponding to the center of the erosion hole in the normal jet cases, had to be determined. However, for all test cases, the location of the point could be inferred from the shape of the smoothed erosion depth distribution with reasonable accuracy.

5.1. *Test case 1: flat aluminum sample*

In the first test case, the normal impingement of a slurry jet against a flat aluminum specimen with density 2700 kg/m^3 was considered. The test parameters were $V_{\mathrm{jet}} \approx 35$ m/s, $C \approx 0.0085$, and $T = 5$ min. An erosion correlation was calibrated for this specific flow condition, employing the improved methodology in the ring-based formulation. The width of the rings used to average the experimental and the numerical results was determined in such a way that 2500 parcel-wall impingements occurred in each ring, since this criterion produced meaningful statistics and a sufficiently high profile resolution.

As already said, the density of the coarse sand particles was 2500 kg/m^3, whereas two difficult-to-evaluate parameters were the grain size distribution and the shape of the grains. In this regard, it has already been noticed that the particles tended to become progressively finer during their recycled use, reducing their mean size of about 12% after 6 hours and 40 minutes of operation. In order to explore whether this effect can adversely affect the accuracy of calibration, the simulations were repeated by sampling the grain size of the injected parcels from four different particle size distributions, namely, the one provided by the retailer and those obtained from the sieve analyses on the brand new sand, after 3 hours and 25 minutes, and after 6 hours and 30 minutes. The results indicated that choosing one particle size distribution instead of another had very little effect on the goodness-of-fit of the $K \cdot f\left(\langle\theta_{\mathrm{P,imp}}\rangle_{\mathrm{ring},i}\right)$ function using Eq. 12. Inspection of the parcel-wall impingement characteristics revealed that such variations in particle size are still too mild to produce significant changes in the behavior of the particle-laden flow. The results presented in the remainder of this section refer to the particle size distribution after 3 hours and 25 minutes of operation, having $d_{\mathrm{p},50} = 0.348$ mm.

Since the coefficient F_s, which appears explicitly in the erosion model formulation considered by Mansouri (Eq. 11), is here included in the calibration constant K, the CFD-based erosion prediction model includes only one parameter related with particle shape. This is the particle shape coefficient in the drag coefficient correlation of Haider and Levenspiel [25], recommended equal to 0.66, 0.76, and 0.86 for highly sharp, semi-rounded, and highly rounded particles, respectively [1]. It is clear that reducing the complexity of the shapes of a mixture of natural sand grains to a single scalar variable is a big challenge, if not impossible. Therefore, it is not surprising to see that the value of φ is a significant source of uncertainty in CFD-based erosion prediction and that, to some extent, φ might be treated as a calibration parameter. As already mentioned in Section 4.2, one of the key ideas of this study is to exploit the combination of CFD and experimental results not only to calibrate an empirical erosion model, but also to gather indications on the proper value of φ to use in the numerical simulations. This is exemplified hereafter.

[Figure 10 about here.]

Figures 10a-c show the ring-based parcel-wall impingement characteristics for the three values of φ, whereas Fig. 10d depicts the experimentally determined ring-averaged erosion depth profile. Whilst the impact velocity distribution is rather insensitive to the value of φ (Fig. 10a) and the impact angles show a only slight increase with increasing φ (Fig. 10b), the number of impacts per ring area is strongly affected by the particle spherical coefficient: in fact, as clearly shown in Fig. 10c, rounded particles are more prone to impinge in the central part of the specimen, whilst sharp grains tend to impinge at a certain distance from the axis of the jet (note that, in order to obtain the number of impacts in each ring, the curves in Fig. 10c should be multiplied by the ring area, which increases with increasaing ring radius). This finding is not surprising because, compared to rounded grains, sharp particles experience higher drag force and, therefore, they have a stronger tendency to follow the fluid streamlines, which spread away from the stagnation region.

[Figure 11 about here.]

The scatter plots in Figs. 11(a-c) show, for the three values of $\varphi = 0.66, 0.76, 0.86$, the ring-averaged parcel impact angle, $\langle\theta_{\mathrm{P,imp}}\rangle_{\mathrm{ring}}$, obtained from the CFD simulations, versus the product $K \cdot f(\langle\theta_{\mathrm{P,imp}}\rangle_{\mathrm{ring}})$, calculated by combining the numerical and experimental results in Eq. 23. The regression curves are also shown. As already evident from visual inspection of the plots, and qualitatively confirmed by the R^2 values, a good fit can be obtained only for $\varphi = 0.66$ (Fig. 11a). Conversely, the trendline is a poor representation of the scattered points for nearly rounded grains with $\varphi = 0.86$ (Fig. 11c). The motivation of this behavior can be found by combining the information reported in Fig. 10 with Eq. 23. When $\varphi = 0.86$, the preferential location of the particle wall impingements, close to the center of the specimen, is not compatible with the observed erosion depth profile. This is quite evident when the attention is turned to point P at $r \approx 10$ mm, where the ring-averaged impact angle is around 11° (Fig. 10b). At this location, there is significant erosion depth (Fig. 10d), but only a limited number of impingements per unit area (black curve in Fig. 10c). When Eq. 23 is applied, such unphysically low value of $\dot{M}_{\mathrm{ring}}/\Delta A_{\mathrm{ring}}$ produces an unphysically high value of $K \cdot f(\langle\theta_{\mathrm{P,imp}}\rangle_{\mathrm{ring}})$, which is clearly visible in Fig. 11c. At the same time, if the point Q of maximum erosion depth is considered, the high $\dot{M}_{\text{ring}}/\Delta A_{\text{ring}}$ (black curve in Fig. 10c) yields low $K \cdot f(\langle\theta_{\text{P,imp}}\rangle_{\text{ring}})$ (Fig. 11c). As a result, the regression curve produces severe underestimation of the erosion depth in P, whereas the erosion depth in Q is overestimated (black curve in Fig. 11d). The fitting is considerably improved when φ is reduced owing to the outward shift of the preferential location of the parcel-wall impingements (Fig. 10c). When φ = 0.66, as characteristics of sharp grains, the maximum erosion depth is accurately captured by the calibrated erosion model (red curve in Fig. 11d).

The considerations above indicate that the accuracy of calibration is strictly related with the value of the particle spherical coefficient. Therefore, it is here recommended to repeat the numerical simulation of the wet direct impact experiment used for calibrating the erosion model three times, with φ equal to 0.66, 0.76, and 0.86, and chose the value of φ for which the predicted erosion depth profile is in closest agreement with the experimental data, by referring, for instance, to the deviation in the maximum value. Apparently, also the goodness-of-fit of the $K \cdot f(\theta_{\text{P,imp}})$ regression model, quantified, for instance, by the R^2 value, might be taken as a criterion to decide the value of φ. However, it will be shown that R^2 is no longer a suitable indicator in the GRE tests and, therefore, referring to the maximum erosion depth appears a better choice. Note that, in any case, the tuning of φ must not be intended in an absolute sense, since the type of grain shape assumed in the simulations (highly sharp, semi-rounded, or highly rounded) must be consistent with the particles used in the experiments, if any information in this sense is available.

As a final note, the mass reduction of the aluminum specimen obtained from the balance was 0.973 g. Volume integration of the experimentally-determined erosion depth profile and subsequent multiplication by the aluminum density yielded 0.744 g. The scope of comparing the two types of measurements was simply to provide some degree of confidence in the reliability of the experimental data. Indeed, the difference between the two values is not negligible, and it was interpreted by considering that, as already discussed in Section 2.3, the uncertainty of the erosion depth measurements is about ±0.1 mm, which is not negligible compared to the measured values in many cells (Figs. 10d). Therefore, the mass loss estimate obtained from the profilometer measurement is expected to be less accurate than that of the balance. The numerically obtained mass losses, calculated through Eq. 22, were 0.827 g, 0.788 g, and 0.925 g, when φ was equal to 0.66, 0.76, and 0.86, respectively.

5.2. Test case 2: curved GRE samples

In the second test case, slurry jet impingements on the curved GRE samples were considered. The calibration of the erosion correlation was made for the following testing conditions: V_{jet}=35.53 m/s, C = 0.0085, and T=5 min. The density of GRE and of the abrasive particles were 2050 kg/m^3 and 2500 kg/m^3, respectively. As far as the size distribution of the abrasive grains is concerned, the only information available came from the tabular data provided by the retailer, previously detailed in Section 2.4, because, unlike for the coarse sand used in the aluminum test, no sieve analysis was made on the fine sand particles of the GRE experiments. Based on the results obtained for the coarse grains, which suggested that moderate changes in the particle size distribution are not likely to affect the accuracy of calibration, the GRE simulations were run by sampling the particle sizes from a log-normal distribution with mean value equal to 0.125 mm, built from the data provided by the retailer. No information could be obtained about the shape of the fine sand particles. Therefore, the particle spherical coefficient φ was treated as a calibration parameter, estimated by combining the experimental and CFD results, as explained in the previous section.

[Figure 12 about here.]

The experimentally-determined erosion depth map over the inner surface of the GRE specimen is depicted in Fig. 12, where the local values have been normalized by the maximum erosion depth to preserve confidentiality. Since the normal impingement against the curved GRE specimen is not an axisymmetric phenomenon, averaging over concentric rings was no longer meaningful, and the general, cell-based approach had to be adopted. Particularly, since the erosion depth measurements were obtained spanning over a Cartesian grid with resolution of 0.5 mm in both directions, the surface cells were squares with edge size of 0.5 mm.

[Figure 13 about here.]

The simulations were repeated three times with φ equal to 0.66, 0.76, and 0.86 and the parcel-wall impingement statistics were calculated over each cell. The results indicated that, as for the first test case, the value of φ has a minor influence on the locally-averaged impact velocity and impact angle (Figs. 13a-f), but it strongly affects the impact number density map (Figs. 13g-k). Particularly, the impacts are mainly concentrated in the central part of the specimen when φ=0.86, whereas they tend to be more uniformly distributed as φ decreases, due to the larger spreading of the trajectories around the stagnation region. It is rather intuitive that, compared to those obtained for φ=0.66 and 0.76, the impact pattern obtained for φ=0.86 (Fig. 13k) is the most likely to produce the experimentally observed erosion map (Fig. 12), thereby suggesting that this is the value of the particle spherical coefficient to be used in the numerical simulations.

[Figure 14 about here.]

In order to confirm this guess, the extended methodology described in Section 4.2 was applied to the three values of φ, thereby determining three different impact angle functions (Figs. 14a,d,g). The R^2 value is very high and almost identical for the three fitting functions, thereby indicating that, unlike in the flat specimen case, this parameter cannot be taken as an indicator of the accuracy of calibration. However, the comparison between the predicted and measured erosion maps clearly reveals that φ=0.86 produces more accurate calibration compared to the two other values of this parameter. This is evident not only by inspecting the maximum predicted erosion depth, which exceeds the experimental one by 36%, 29%, and 22% for φ equal to 0.66, 0.76, and 0.86 (Figs. 14b,e,h), but also from the shape of the erosion crater, which, as φ decreases, tends to be elongated along the horizontal axis and deviates from the evidence (Figs. 14c,f,k). Further looking at Figs. 14c,f,k, it can be noted that, unlike the experimentally-determined ones, the predicted erosion profiles show two local peaks for all values of φ. This is due to the fact that, owing to the drag and pressure gradient forces, the trajectories are pushed away from the stagnation region, and, therefore, the maximum impact number density is found at a certain distance from the center of the specimen. This effect is reduced for φ=0.86, but it cannot be completely avoided. As a consequence, a U-shaped crater is impossible to obtain with the current CFD model. Given the influence of φ on the configuration of the particle trajectories, it would not be surprising to find better match with the observed erosion hole with a higher φ. Nonetheless, values of φ larger than 0.86 would be out of the recommended range for natural sands [1], and, therefore, they might produce an unphysical solution.

[Figure 15 about here.]

As explained in Section 4.2, one of the proposed modifications to the methodology of Masouri consists in elevating the impact velocity modulus to power n before cell-averaging instead of applying the cell-average operator first. The motivation behind this change was to make the procedure consistent with the E-CODE library used for processing the parcel-wall impingement characteristics produced as output by Fluent. As a practical counterpart to the mathematical derivation in Section 4.2, cell-averaging the impact velocity modulus after elevating to power n was found to have a positive effect on the accuracy of calibration for the GRE test case. This is evident in Fig. 15b, which is the same as Fig. 14k including also the two green-colored profiles obtained when the cell-averaged impact velocity is applied to power n. The erosion depth distribution corresponding to the green-colored profiles, shown in Fig. 15a, indicates a maximum predicted erosion depth around 36% higher than the maximum measured value. The underestimation is therefore much worse compared to that obtained when the elevation to power n is performed before cell-averaging (Fig. 14h).

[Figure 16 about here.]

The results discussed so far indicate that, although the concept behind the calibration procedure of Mansouri et al. [18, 19] and its local generalization is rather straighforward, achieving accurate predictions might not be simple even for the calibration case. In fact, the predicted parcel-wall impingement characteristics must be necessarily consistent with the observed erosion depth distribution, and this requires both careful control of the experimental tests and reliable modelling of the particle-laden flow close to solid walls. Nonetheless, it is observed that, despite the differences in the location of the maximum erosion, the case-specific correlation shows much better performance compared to the comprehensive erosion model of Oka et al. [8, 9], calibrated with respect to dry direct impact test experiments. Figure 16 shows the erosion depth map predicted by the erosion model of Oka et al. [8, 9], and it clearly reveals that, even with φ=0.86, this model does not produce a wear pattern consistent with the experiment. The estimates in Fig. 16 refer to a Vickers hardness equal to 30 GPa, but a sensitivity analysis revealed that the shape of the erosion hole is substantially unaffected by the value of this parameter.

The comparison between calculated and measured erosion characteristics can be extended also to the overall mass loss. If the mass reduction obtained from the balance is attributed a unit value, that obtained from the integration of the experimentally determined erosion map was 0.754. Referring to the same normalization, the calculated values for φ equal to 0.66, 0.76, and 0.86 were 2.197, 1.461, and 0.925, respectively. This further confirms the conclusions reached by inspecting the surface of the erosion crater in Fig. 14, namely, that, compared to 0.66 and 0.76, 0.86 is the most suitable value of particle spherical coefficient for the current test case.

[Figure 17 about here.]

The calibrated erosion model for φ=0.86 was finally employed to simulate the two other experimental tests, in which the testing time was increased keeping all other parameters essentially constant. Figures 17a,b are analogous to Fig. 14k for T equal to 15 and 30 minutes, respectively. These plots do not represent a validation since, when using a one-way coupled steady-state CFD model, the wear profiles scales linearly with testing time and concentration and, therefore, the CFD curves in Figures 17a,b can be immediately obtained from those in Fig. 14k. Nonetheless, it is interesting to observe that, as the testing time increases, the CFD model progressively overestimates the measured erosion depth, indicating that the erosion hole deepens less-than-linearly with time. Such behaviour is well known in the literature, and it was observed, for instance, by Nguyen et al. [22] when performing normal slurry jet impingement tests on a flat stainless steel sample. With the aid of CFD simulations, Nguyen et al. [22] argued that the deviation from the steady-state erosion was the consequence of the changes in the particle-laden flow produced by the eroding surface, and this interpretation was recently confirmed by Messa and Malavasi [32], Parsi et al. [31] and Duarte and De Souza [33]. Such unsteady effect cannot be captured by the steady-state CFD model employed in the present study and, therefore, the results in Figs. 17a,b are not surprising. The erosion profiles in Figs. 17a,b have a clear correspondence with the time evolution of the overall mass reduction, shown in Figs. 17c. Whereas the predicted mass loss obviously linearly increases with time, both experimental data series (obtained using the balance and from volume integration of the profilometer data) increase less than linearly, in agreement with the earlier findings of Nguyen et al. [22].

6. Conclusions and future developments

The present study presents an improved formulation of a methodology for the calibration of empirical erosion models previously introduced by Mansouri et al. [18, 19], which relies on a combination of experimental data and CFD results of a normal wet direct impact test. In the authors' opinion, the methodology might have a strong impact on the engineering simulation of slurry erosion since it represents a practical compromise to obtain, at least for specific flow conditions, reliable erosion predictions, avoiding, on the one hand, the high computational burden of micro-scale erosion simulations solving for the physical laws of damage and fracture mechanics and, on the other hand, the inherent uncertainty of mechanistic erosion models and empirical erosion models based on dry direct impact tests.

As a result of an extensive computational work and referring to original experimental data, the upgraded methodology allows overcoming some well-known drawbacks of CFD-based erosion prediction [31]. The main achievements are as follows.

- It has been demonstrated that the consistency between the parcel-wall impingement characteristics, predicted by the CFD model, and the measured erosion distribution is a necessary requirement to achieve accurate calibration of the erosion correlation. In this regard, the role played by the particle spherical coefficient, φ, in the drag coefficient correlation is fundamental. It has been proposed to take the calibration accuracy of the erosion model as a criterion to decide the proper value of φ, which is very difficult to quantify for natural abrasives. Particularly, it has been recommended to run the numerical simulations for three reference values of particle spherical coefficient (0.66, 0.76, and 0.87), thereby determining three different erosion correlations, and identify the value of φ which produces the lowest deviation from the experiments in terms of maximum erosion depth. It has been also shown that, in some situations (but not always), the goodness-of-fit of the regression impact angle curve, quantified by the R^2 value, might be also taken as a criterion to identify the most suitable value of φ. This contributed to widening the scope of the combined CFD/experimental methodology, which does not only allow calibrating an empirical erosion formula, but it also gives some indication on the proper value of φ to be set in the CFD model.

- In the new methodology, the coefficient F_s does no longer appear explicitly in the erosion formula but it is included in the coefficient K. This avoids the need to handle two different parameters related with particle shape, namely, φ and F_s, which are not independent with each other as they are associated with the same geometrical feature of the particle phase. Additionally, removing F_s clearly underlines that the developed erosion formula cannot be applied to other particles than those used for the calibration.

- In the upgraded equation for the calibration of the impact angle function (Eq. 21), the impact velocity term is elevated to power n before cell-averaging, and not after cell-averaging as in the original formulation. This made the procedure more consistent with the post-processing of the parcel-wall impact data made by the E-CODE library, resulting in an improved calibration accuracy.

- In CFD model, the parcel-wall impingement characteristics were not evaluated at the wall boundaries, as implied by the point-particle approximation, but at an upstream distance from the wall equal to half of the particle diameter, following a procedure previously developed by two authors of this study [29]. This allowed not only improving the accuracy of the numerical evaluation of the impacts, but it also reduced their dependence upon the near-wall mesh resolution and the near-wall treatment method.
- A ring-based formulation of the methodology was proposed to make its application to statistically axi-symmetric flows more straightforward.

Although the present study represents a step forward in the development of reliable and practically useful CFD-based erosion prediction models, two tasks remain unresolved and have been shelved for future research. The former is the characterization of the velocity exponent n, which was here assumed equal to 2.4 as initially recommended by Mansouri et al. [18, 19] but it is likely to be dependent on the materials involved in the process. Criteria for deciding the proper value of n should be established, and this requires disposing of experimental data for different jet velocities, abrasive particles, and target materials. The second drawback of this work is the lack of a validation of the calibrated erosion correlation. This study focused on the calibration phase and showed that even achieving a good calibration accuracy is more challenging than it might appear at first sight. Given the experimental database available, only exploring the effect of testing time was possible. However, even if the findings are in line with previous experimental and numerical results, this did not represent a real validation, owing to the assumptions underlying the CFD model used which make the CFD predictions at different testing time not independent from each other. Validating the predictions of the calibrated formula against other experimental tests (e.g. jet impingements at different velocity and nozzle-to-specimen angles, or different types of flows involving the same combination of materials) will be definitely required to demonstrate the effectiveness of the methodology for engineering purposes.

Acknowledgements

The numerical simulations performed in this study were run on the GALILEO supercomputer at CINECA as part of the ISCRA research project IsC78 (MASS - Modelling Anisotropic flows in Single-phase and Slurry conditions). Authors would like to acknowledge Cristina Tedeschi from the Laboratory for Diagnostic and Investigation on Built Heritage Materials of Politecnico di Milano, who scanned the specimens and performed the sieve analysis of the abrasive particles used in the aluminum experiments, ENI S.p.A., which partially supported this research, and NOV Wellbore Technologies, which provided the GRE specimens.

References

[1] G.V. Messa, S. Malavasi, The effect of submodels and parameterization in the simulation of abrasive jet impingement tests, Wear 370–371 (2017) 59–72.

[2] C.T. Crowe, J.D. Schwarzkopf, M. Sommerfeld, Y. Tsuji, Multiphase Flows with Droplets and Particles, CRC Press, Boca Raton, US-FL, 2012.

[3] C.A.R. Duarte, F.J. de Souza, R. de Vasconcelos Salvo, V.F. dos Santos, The role of inter-particle collisions on elbow erosion, Int. J. Multiphase Flow 89 (2017) 1–22.

[4] S. Laín, M. Sommerfeld, Numerical prediction of particle erosion of pipe bends, Advanced Powder Technol 30 (2019) 366–383.

[5] Y.F. Wang, Z.G. Yang, A coupled finite element and meshfree analysis of erosive wear, Tribol Int 42 (2009) 373–377.

[6] C. Zheng, Y. Liu, C. Chen, J. Qin, S. Zhang, Finite element analysis on the dynamic erosion process using multiple-particle impact model, Powder Technol 315 (2017) 163–170.

[7] J. Di, S.S. Wang, L. Zhang, L.X. Cai, Y.H. Xie, Study on the erosion characteristics of boride coatings by finite element analysis, Surf Coat Technol 333 (2018) 115–124.

[8] Y.I. Oka, K. Okamura, T. Yoshida, Practical estimation of erosion damage caused by solid particle impact. Part 1: Effects of impact parameters on a predictive equation, Wear 259 (2005) 95–101.

[9] Y.I. Oka, T. Yoshida, Practical estimation of erosion damage caused by solid particle impact. Part 2: Mechanical properties of materials directly associated with erosion damage, Wear 259 (2005) 102–109.

[10] S. Leguizamón, E. Jahanbakhsh, A. Maertens, S. Alimirzazadeh, F. Avellan, A multiscale model for sediment impact erosion simulation using the finite volume particle method, Wear 392–393 (2017) 202–212.

[11] S. Leguizamón, E. Jahanbakhsh, S. Alimirzazadeh, A. Maertens, F. Avellan, Multiscale Simulation of the Hydroabrasive Erosion of a Pelton Bucket: Bridging Scales to Improve the Accuracy, Int J Turbomach Propuls Power 4 (2019), 9 pages.

[12] S. Leguizamón, S. Alimirzazadeh, E. Jahanbakhsh, F. Avellan, Multiscale simulation of erosive wear in a prototype-scale Pelton runner, Renew. Energ. 151 (2020) 204–215.

[13] I. Finnie, Erosion of surfaces by solid particles, Wear 3 (1960) 87–103.
[14] J.G.A. Bitter, A study of erosion phenomena. Part I, Wear 6 (1963) 5–21.
[15] J.G.A. Bitter, A study of erosion phenomena. Part II, Wear 6 (1963) 169–190.
[16] C. Huang, S. Chiovelli, P. Minev, J. Luo, K. Nandakumar, A comprehensive phenomenological erosion model for erosion of materials in jet flow, Powder Technol 187 (2008) 273–279.
[17] H. Arabnejad, A. Mansouri, S.A. Shirazi, B.S. McLaury, Development of mechanistic erosion equation for solid particles, Wear 332–333 (2015) 1044–1050.
[18] A. Mansouri, H. Arabnejad, S.A. Shirazi, B.S. McLaury, A combined CFD/experimental methodology for erosion prediction. Wear 332–333 (2015) 1090-1097.
[19] A. Mansouri, A combined CFD–experimental method for developing an erosion equation for both gas–sand and liquid–sand flows. PhD thesis, The University of Tulsa, US-OK, 2016.
[20] D.R. Lide, CRC Handbook of chemistry and physics, CRC Press, Taylor & Francis, Boca Raton, US-FL, 2016.
[21] A. Mansouri, S.A. Shirazi, B.S. McLaury, Experimental and numerical investigation of the effect of viscosity and particle size on the erosion damage caused by solid particles, in: Proceeding of 2014 ASME Joint US-European Fluids Engineering Division Summer Meeting, Chicago, IL, 2014. Paper No. FEDSM2014-21613.
[22] V.B. Nguyen, Q.B. Nguyen, Z.G. Liu, S. Wan, C.Y.H. Lim, Z.W. Zhang, A combined numerical–experimental study on the effect of surface evolution on the water–sand multiphase flow characteristics and the material erosion behavior. Wear 319 (2014) 96–109.
[23] H.K. Versteeg, W.Malalasekera, An Introduction to Computational Fluid Dynamics - The Finite Volume Method, Pearson Prentice Hall, Harlow, UK, 2007.
[24] ANSYS FLUENT Theory Guide, ANSYS Inc., Southpoint, 275 Technology Drive, Canonburg, PA15317, USA, 2013.
[25] A. Haider, O. Levenspiel, Drag coefficient and terminal velocity of spherical and non-sperical particles, Powder Technol. 58 (1989) 63–70.
[26] R. Mei, An approximate expression for the shear lift force on a spherical particle at finite Reynolds number, Int. J. Multiph. Flow 18(1992) 145–147.
[27] H. Schlichting, Boundary-Layer Theory, McGraw-Hill, New York, 1960.
[28] A. Forder, M. Thew, D. Harrison, A numerical investigation of solid particle erosion experienced within oilfield control valves, Wear 216 (1998) 184–193.
[29] G.V. Messa, Y. Wang, Importance of accounting for finite particle size in CFD-based erosion prediction, in: Proceedings of 2018 ASME Pressure Vessels and Piping Conference, Prague, CZ, 2018. Paper No. PVP2018-84248.
[30] J. Zhang, B.S. McLaury, S.A. Shirazi, Application and experimental validation of a CFD based erosion prediction procedure for jet impingement geometry, Wear 394–395 (2018) 11–19.
[31] M. Parsi, A. Jatale, M. Agrawal, P. Sharma, Effect of surface deformation on erosion prediction, Wear 430 (2019) 57–66.
[32] G.V. Messa, S. Malavasi, A CFD-based method for slurry erosion prediction, Wear 398–399 (2018) 127–145.
[33] C.A.R. Duarte, F.J. de Souza, Dynamic mesh approaches foreroded shape predictions, Wear (2020), doi: https://doi.org/10.1016/j.wear.2020.203438.

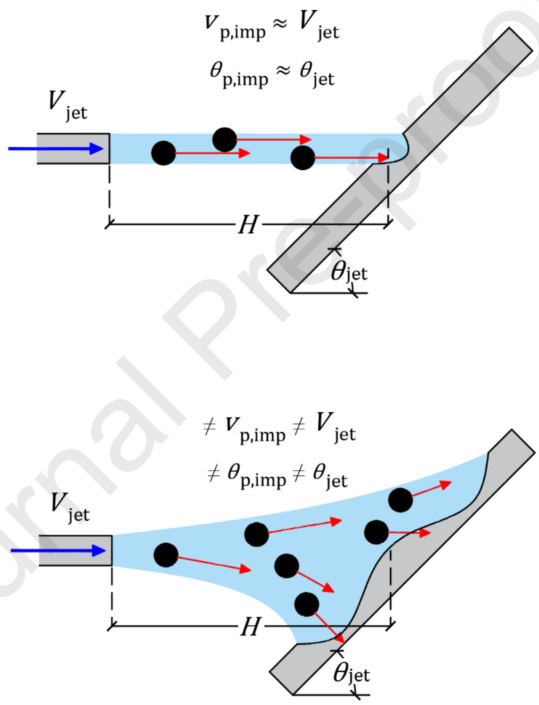

(a)

(b)

Fig. 1. Sketch of (a) a dry direct impact test and (b) a wet direct impact test.

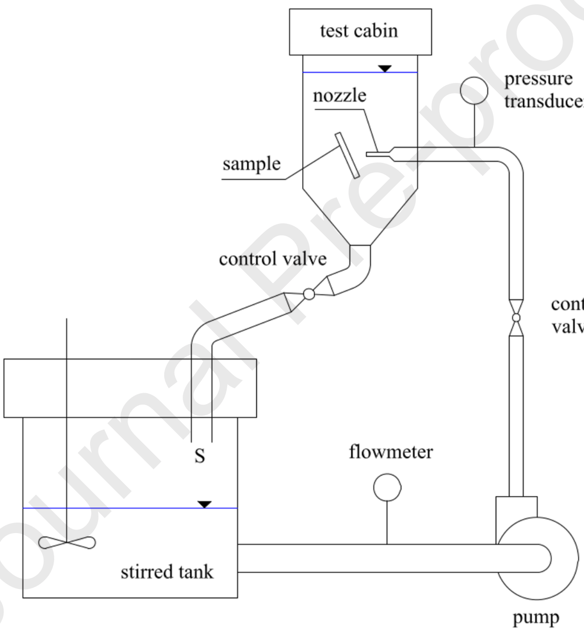

Fig. 2. Simplified sketch of the wet direct impact test facility at the Hydraulic Laboratory of Politecnico di Milano.

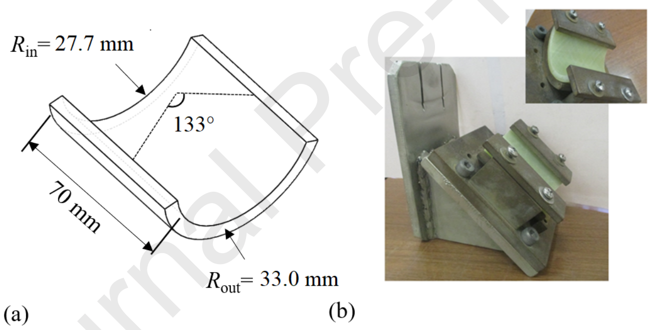

Fig. 3. (a) the GRE specimens and (b) their clamping holder.

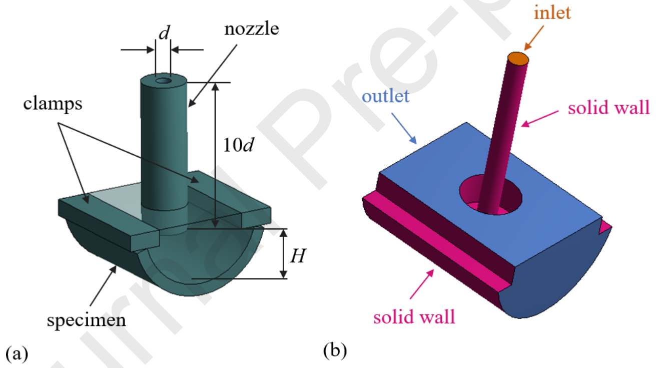

Fig. 4. (a) computational domain and (b) boundary conditions for the curved GRE specimen case.

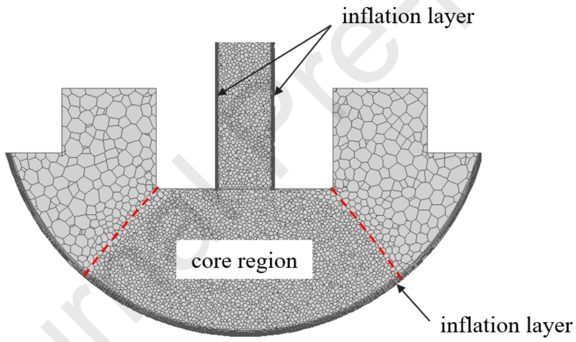

Fig. 5. restricted view of the discretization of the mid plane for the curved GRE specimen case.

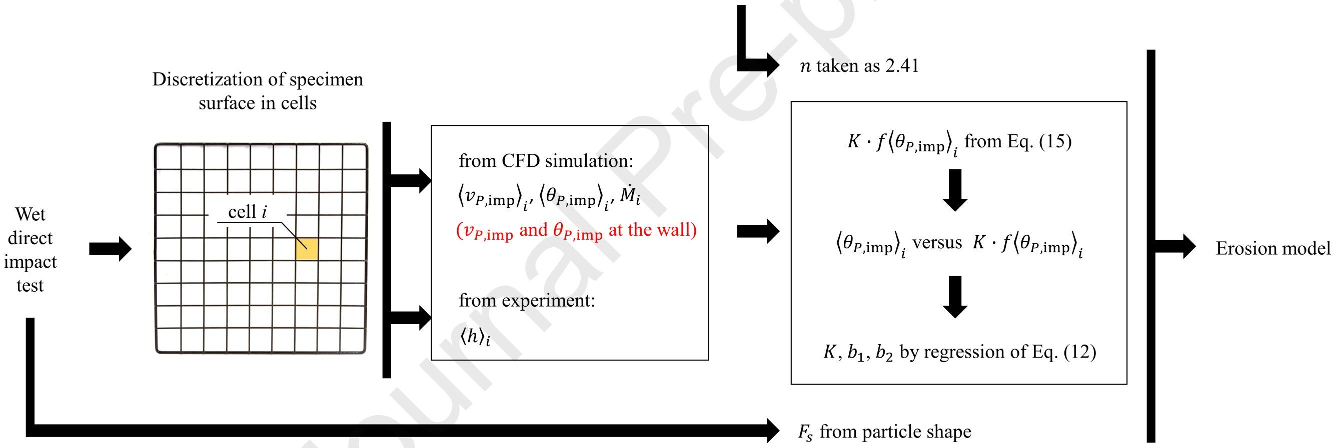

Fig. 6. Flowchart of the original methodology of Mansouri [19].

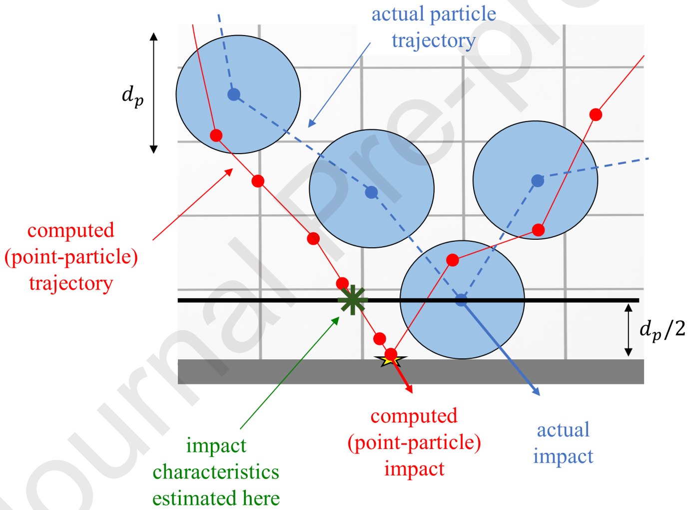

Fig. 7. evaluation of the parcel-wall impingement characteristics according to the strategy of Messa and Wang [29].

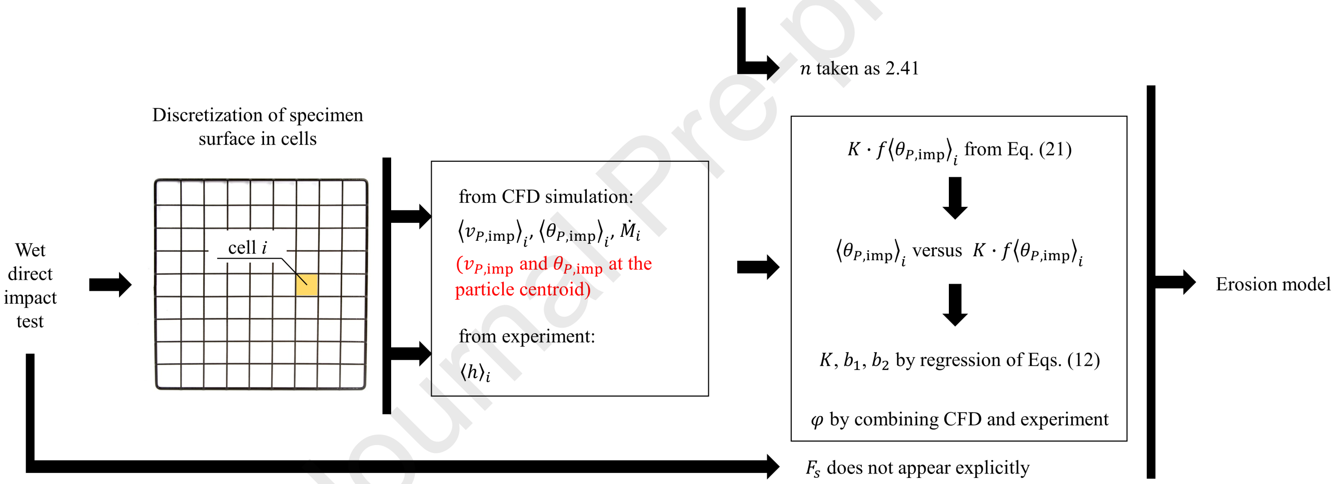

Fig. 8. Flowchart of the improved methodology.

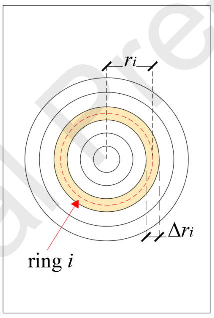

Fig. 9. subdivision of the surface of the specimen into concentric rings.

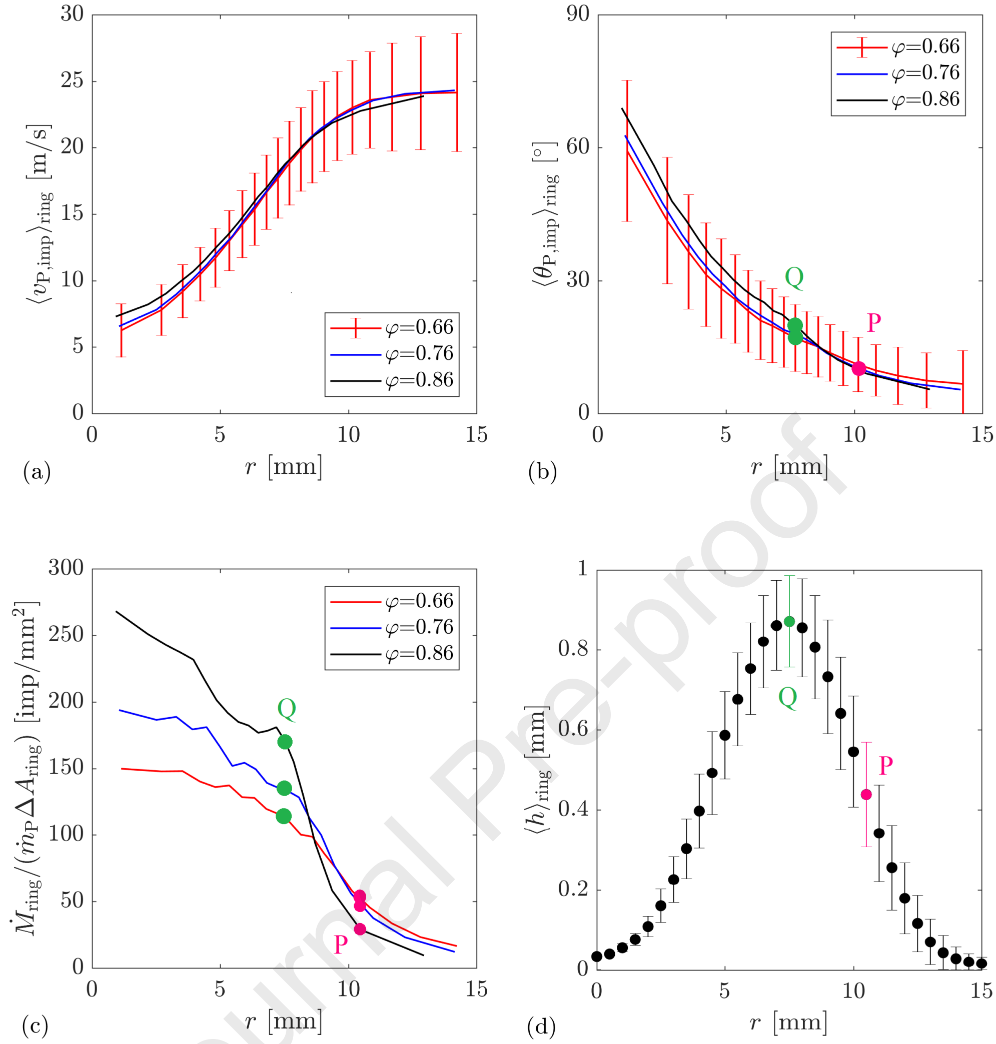

Fig. 10. (a,b,c) output of the Eulerian-Lagrangian simulations: ring-averaged profiles of (a) mean parcel-wall impact velocity, (b) mean parcel-wall impact angle, (c) impact number density. (d) experimentally-determined ring-averaged erosion depth profile. In plots (b,c), the error bars, equal to the standard deviation over the impingements occurring in each ring, are similar for the three values of φ, and they have been plotted only for $\varphi = 0.66$ for the sake of clarity. In plot (d), the vertical bars represent the azimuthal variability of the erosion depth over each ring.

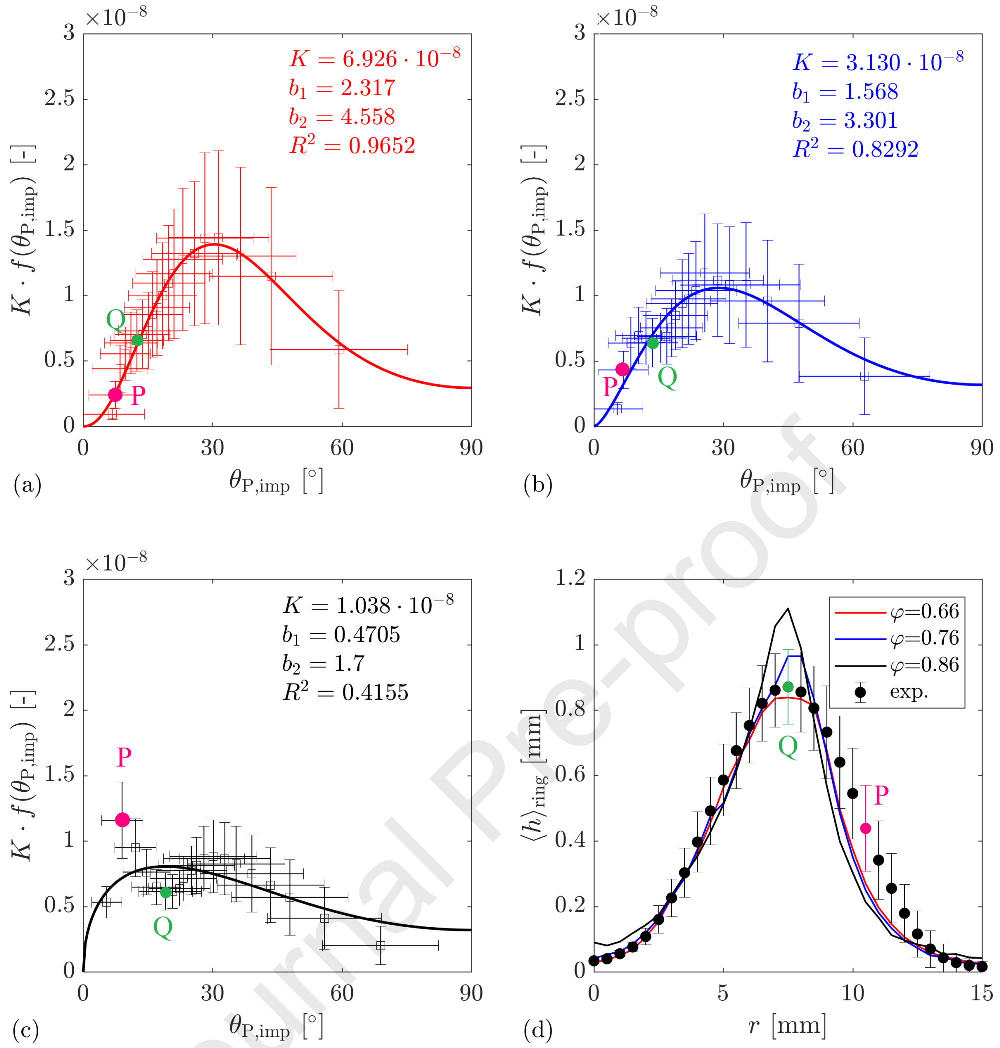

Fig. 11. calibration of the impact angle function $K \cdot f(\theta_{\mathrm{P,imp}})$ for φ equal to (a) 0.66, (b) 0.76, and (c) 0.86. (d) erosion depth profiles obtained from the three regression curves and from the ring-averaged profilometer data. The horizontal and vertical bars in plots (a-c) indicate the variability of the $\theta_{\mathrm{P,imp}}$ and $K \cdot f(\theta_{\mathrm{P,imp}})$ values in each ring, respectively. In plot (d), the vertical bars represent the azimuthal variability of the erosion depth over each ring.

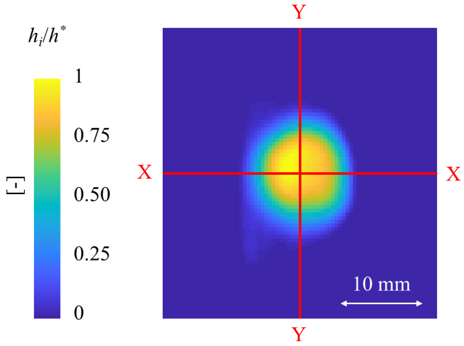

Fig. 12. experimentally-determined wear depth distribution over the inner surface of the GRE specimen for case V_{jet}=35.53 m/s, C = 0.0085, and T=5 min. In order to preserve confidentiality, the data have been normalized with respect to the maximum value, referred to as h^*. Lines XX and YY represent the horizontal and vertical axes of the specimen.

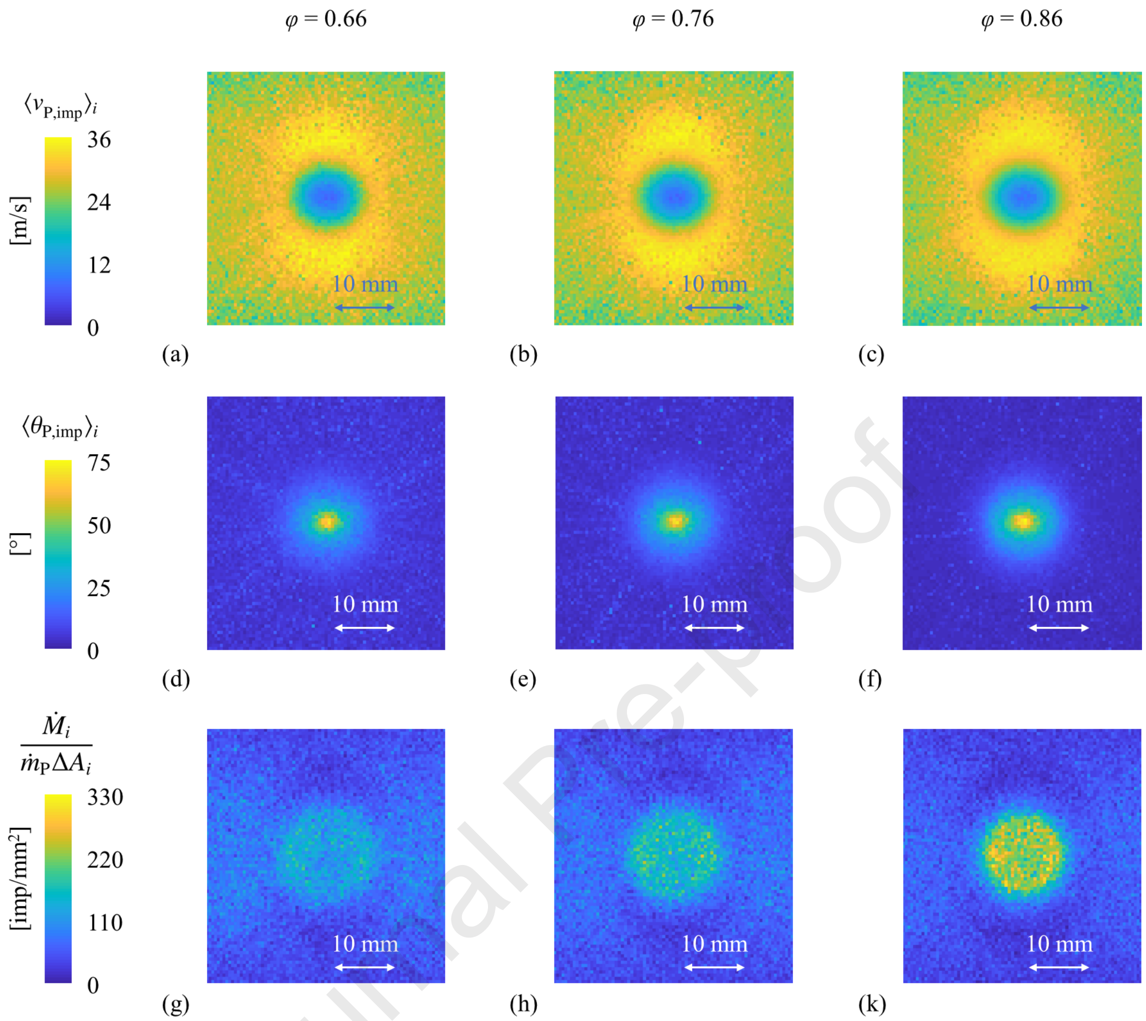

Fig. 13. calculated parcel-wall impingement statistics over the inner surface of the GRE specimen for case V_{jet}=35.53 m/s, C = 0.0085, and T=5 min: (a-c) locally averaged impact velocity (d-f) locally averaged impact angle (g-k) impact number density. The columns from left to right refer to increasing values of the particle spherical coefficient.

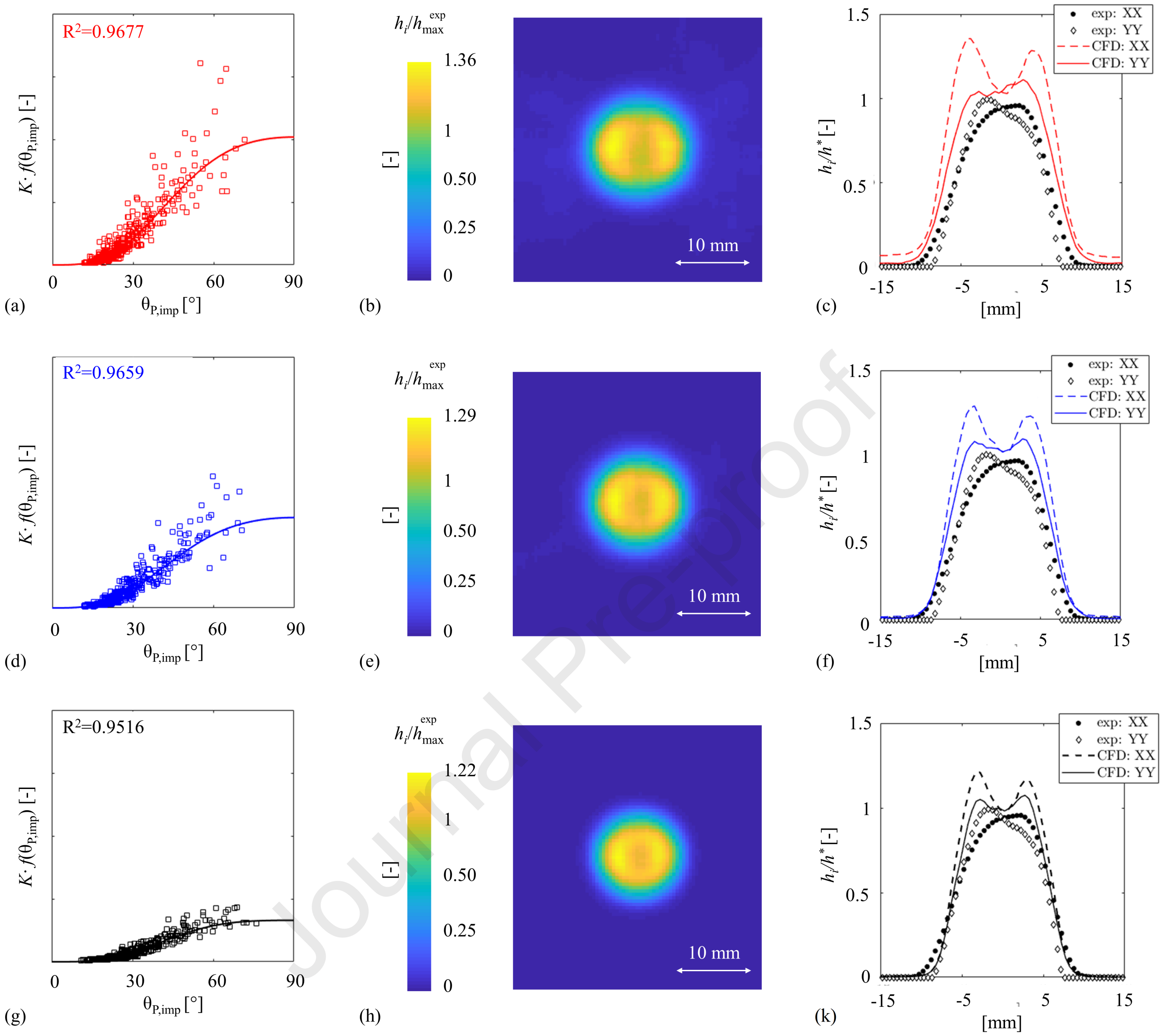

Fig. 14. results of the second test case for φ equal to (a-c) 0.66, (d-f) 0.76, and (g-k) 0.86. Left column: calibration of the impact angle function $K \cdot f(\theta_{P,imp})$ by combining the experimentally determined erosion depth map in Fig. 12 and the calculated parcel-wall impingement statistics in Fig. 13. The limits of the vertical axes are the same for all plots, but they have not been shown to preserve confidentiality. Center column: predicted erosion depth map, normalized by the maximum experimental value in Fig. 12. Right column: comparison of predicted and measured erosion depth profiles along the horizontal (XX) and the vertical (YY) axes, normalized by the maximum experimental value in Fig. 12.

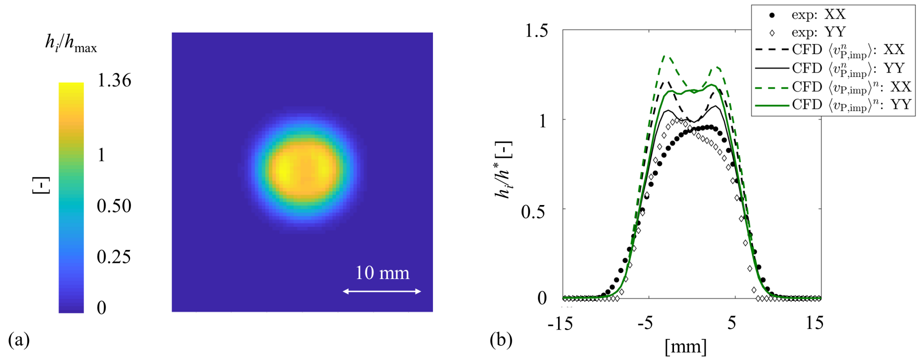

Fig. 15. (a) analogous of Fig. 14h when, in Eq. 21, the impact velocity is elevated to power *n* after cell averaging; (b) analogous of Fig. 14k including also the erosion depth profiles obtained by applying Eq. 21 with impact velocity elevated to power *n* after cell averaging.

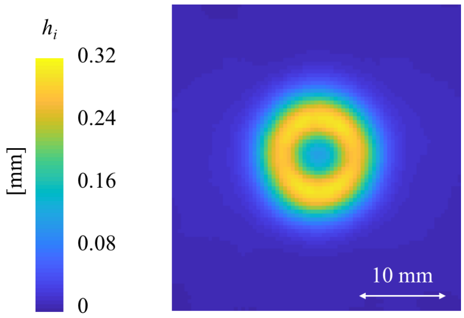

Fig. 16. wear depth distribution over the inner surface of the GRE specimen for case $V_{\rm jet}$=35.05 m/s, C = 0.0085, and T=5 min obtained by applying the erosion model of Oka et al. [8, 9] with Vickers hardness of 30 GPa.

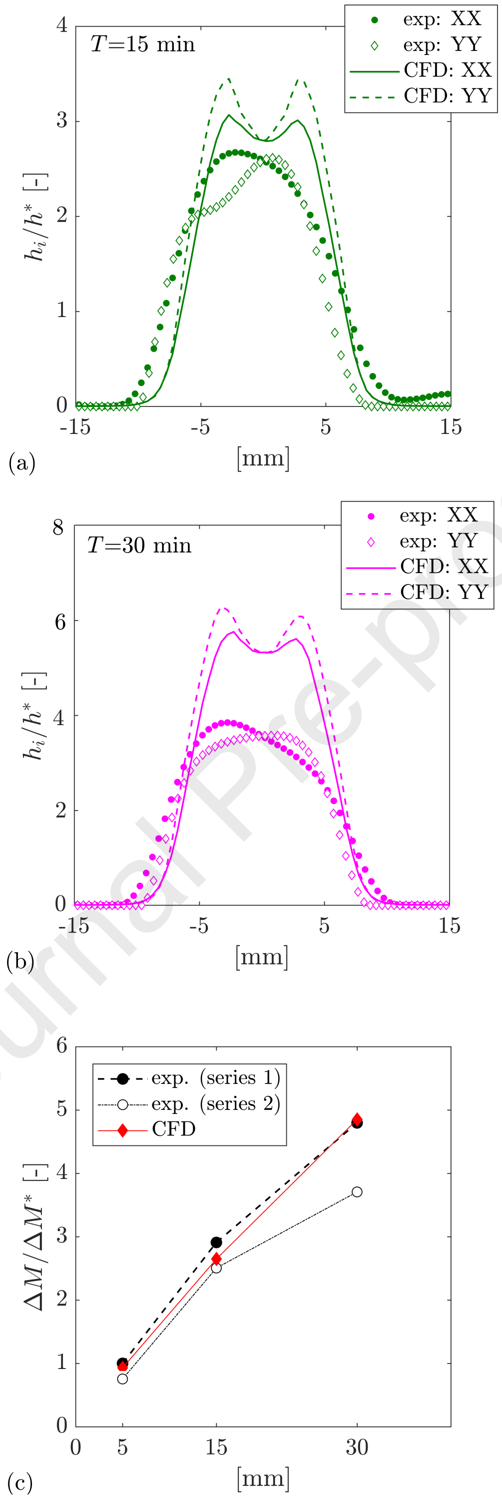

Fig. 17. (a,b) analogue of Figs. 14c,f,k for testing time equal to (a) 15 minutes and (b) 30 minutes. The normalization factor, h^*, is the maximum measured erosion depth for the 5 minutes test. (c) Overall mass loss versus time for the three test case. Series 1 and 2 are the values obtained from the balance and from volume integration of the profilometer data, respectively. The normalization factor, ΔM^*, is the data obtained from the balance for the 5 minutes test.

Eroding sample	Erosion depth Mass of specimen Target density, ρ_t	$\approx$0.1 mm $\pm$3.5 mg $\pm$50 kg/m^3 (GRE samples)
Abradant	Particle density, ρ_p Mean particle diameter, $d_{p,50}$	Substantially ineffective Reduced by about 13% during the test on aluminum specimen
Testing conditions	Jet bulk-mean velocity, V_{jet} Nozzle-to-specimen angle, θ_{jet} Nozzle-to-specimen distance, H Solid volume fraction, C	$\pm$2.4% $\pm$1° $\pm$0.05 mm $\pm$0.001

Table 1
Key elements of the uncertainty analysis.

Eroding sample	Type of material	Aluminum alloy EN AW-608	Glass Reinforced Epoxy (GRE)
	Target density, ρ_t [kg/m^3]	2700	2050±50
	Surface of specimen	Flat	Curved
	Dimensions of specimen [mm]	80x60x5	See Fig. 3a
Abradant	Type of material	Coarse silica sand	Fine silica sand
	Particle density, ρ_p [kg/m^3]	2500	2500
	$d_{p,10}$ [mm]	0.25	0.075
	$d_{p,50}$ [mm]	0.35	0.125
	$d_{p,90}$ [mm]	0.46	0.200
Testing conditions	Jet velocity V_{jet} [m/s]	35.53±0.71	≈35
	Nozzle-to-specimen angle, θ_{jet} [°]	90±1	90±1
	Nozzle-to-specimen distance, H [mm]	12.7±0.05	12.7±0.05
	Solid volume fraction, C [-]	0.0085±0.001	0.0076 to 0.0085
	Testing time, T [min]	5	5, 15, 30

Table 2
Summary of the experimental conditions.

Particle-laden flow	Phase coupling regime	One-way coupling
Carrier fluid	Flow equations Turbulence model Near-wall treatment	RANS RSTM Scalable wall function
Particle phase	Forces included in the parcel equation of motion Particle turbulent dispersion model Parcel-wall resistution coefficients Evaluation of impact charateristics	Drag force (Haider and Levenspiel [25]) Lift force (Mei [26]) Pressure gradient force Virtual mass force C_{vm}=0.5 Random Walk Model Forder et al. [28] At particle centroid

Table 3
Modelling features of the Eulerian-Lagrangian model. Unspecified settings are the default ones in Ansys Fluent version 19.2.

Carrier fluid	Type of mesh	Polyhedral with inflation layer
	Number of inflation layers [-]	5
	First inflation layer thickness [mm]	0.05
	Number of cells [millions]	≈1.26 (test case 1), ≈1.45 (test case 2)
	Type of solver	Coupled, pressure-based
	Gradient discretization method	Green-Gauss Node-based
	Pressure discretization scheme	PRESTO!
	Discretization scheme for all other variables	Second Order Upwind
	Convergence criterion	10^{-4} (normalized residuals)
	Under-relaxation factors	Default settings
Particle phase	Tracking mode	Steady-state
	Number of tracked parcels [-]	50000
	Tracking parameters [-]	Default settings

Table 4
Key numerical settings of the CFD model. Unspecified settings are the default ones in Ansys Fluent version 19.2.

An improved CFD/experimental combined methodology for the calibration of empirical erosion models (Abstract Ref. number: WEAR2021_0102)

Gianandrea Vittorio Messa*, Yongbo Wang, Marco Negri, Stefano Malavasi

DICA, Politecnico di Milano, Piazza Leonardo da Vinci, 32, 20133 Milano, Italy

Highlights

- An existing CFD/experimental methodology for calibrating erosion models is improved
- The new methodology allows for higher accuracy of calibration
- It also allows for fine tuning of the particle spherical coefficient
- The methodology is applied to slurry jet tests on flat and curved samples

*Corresponding author. Tel. +39 02 2399 6287

Email addresses: gianandreavittorio.messa@polimi.it (Gianandrea Vittorio Messa), yongbo.wang@polimi.it (Yongbo Wang), marco.negri@polimi.it (Marco Negri), stefano.malavasi@polimi.it (Stefano Malavasi)

Declaration of interests

☒ The authors declare that they have no known competing financial interests or personal relationships that could have appeared to influence the work reported in this paper.

☐The authors declare the following financial interests/personal relationships which may be considered as potential competing interests: